Measurement of Air Temperatures and Velocities in the Fiber Glass Forming Environment

by

Brett M. McKeone

Submitted to the Department of Mechanical Engineering in
Partial Fulfillment of the Requirements for the Degrees of

Master of Science in Mechanical Engineering
Bachelor of Science in Mechanical Engineering

at the

Massachusetts Institute of Technology

June 1999

Author_____
Department of Mechanical Engineering
May 7, 1999

Certified by_____
John H. Lienhard V
Associate Professor of Mechanical Engineering
Thesis Supervisor

Accepted by_____
Ain Sonin
Chairman of Graduate Studies
Department of Mechanical Engineering

Measurement of Air Temperatures and Velocities in the Fiber Glass Forming Environment

by
Brett M. McKeone

Submitted to the Department of Mechanical Engineering on May 7, 1999
in Partial Fulfillment of the Requirements for the Degrees of
Master of Science in Mechanical Engineering
Bachelor of Science in Mechanical Engineering

Abstract

The manufacture of continuous strand fiber glass is accomplished by draining molten glass through an array of small orifices in a heated bushing plate and then drawing the glass onto a winder. Upon exiting the orifices, the fibers pass through a cloud of atomized water to assist in the cooling of the fibers and then over a surfactant applicator before they are wound.

The rate at which the cooling of the fibers occurs relies heavily on the operating conditions used in the process. This report deals with measurements made in a scaled-down process using a variety of different operating conditions. Experimental data on air temperatures and velocities were recorded within the forming environment without water sprays.

Trials were run using an apparatus similar to one used in production, but of a much smaller scale. In production, a granular batch is continuously fed into a furnace, melted, mixed, and sent down a slightly downward sloping channel, via gravity. A series of electrically heated bushings, each with hundreds of tips, lies below the channel, allowing the molten glass to drain. The apparatus used in this study, however, consisted of one isolated nine-tip bushing with a small well above it. Glass marbles were placed in the well, and the system was electrically heated, melting the glass and allowing it to drain from the well through the bushing tips.

The speed at which the fiber was drawn was varied, as was the bushing temperature. It was found that fiber diameter, which is information essential for predicting cooling rates, varies with both of these parameters, but is more heavily influenced by bushing temperature. By running the process at a constant bushing temperature, while using a series of fiber speeds, it was found that varying the speed of the fiber noticeably changes the temperature field in the forming environment. By increasing the fiber speed from 12.2 m/s to 21.3 m/s there are more noticeable temperature peaks surrounding the individual fibers, indicating significant differences in convective cooling rates as fiber speed is varied. Similar trends are seen for a constant fiber speed as the bushing temperature is increased from 1505 K to 1533 K, though the differences are not as dramatic. In addition it was necessary to correct temperature measurements using a theoretical heat transfer model, to account for error due to radiative heating of the thermocouple from the bushing plate and conductive heat loss through the thermocouple leads.

Air velocity measurements were also taken using the same series of operating conditions. Increasing the fiber speed resulted in noticeably higher air velocities; increasing the bushing temperature also raised air velocity, although the change was less significant.

Thesis Supervisor: John H. Lienhard V
Title: Associate Professor of Mechanical Engineering

Acknowledgments

I would like to thank PPG Industries for sponsoring the research presented in this thesis. Dr. R. Allen Roach and Dr. Jerome A. Bergman were extremely helpful in sharing their expertise in the field of glass fiber manufacturing. Their assistance in guiding the research , answering questions, and their help in overcoming some major obstacles is greatly appreciated.

In addition, I would like to thank Professor John H. Lienhard V for his guidance and assistance in developing the presented work. I am very thankful for his active involvement in the research and especially his patience during difficult times.

Contents

List of Figures

1. Introduction

The fiber glass forming process involves a combination of extrusion and pultrusion of molten glass through an array of orifices in a row of platinum-iridium bushings. The bushings are heated electrically and maintained at a constant temperature of around 1500 K. In production, a constant glass depth in the forehearth above the row of bushings of approximately 0.3 m is maintained, which ensures a constant pressure at each orifice. The glass is pulled through the orifices by a take-up reel as well as pushed through by the pressure caused by the depth of the molten glass above the bushing. This causes the glass to neck until it solidifies to its final diameter, which is on the order of 10 μm. The resulting filaments are brought together and passed across a surfactant applicator, which binds the filaments together into a single fiber. The fiber is then pulled onto a winder.

Radiation and convection are major modes of heat transfer from the filaments to the forming environment. The cooling of the filaments is assisted using a row of water-

atomizing nozzles and forced convection using conditioned air flows from a duct located above the row of nozzles. The glass solidifies at a temperature of 1390 K and then must cool to a temperature below 367 K before the surfactant is applied. The filaments are typically drawn at rates varying between 3 m/s and 30 m/s over a length on the order of 1 m. Fig. 1.1 illustrates the process used in production.

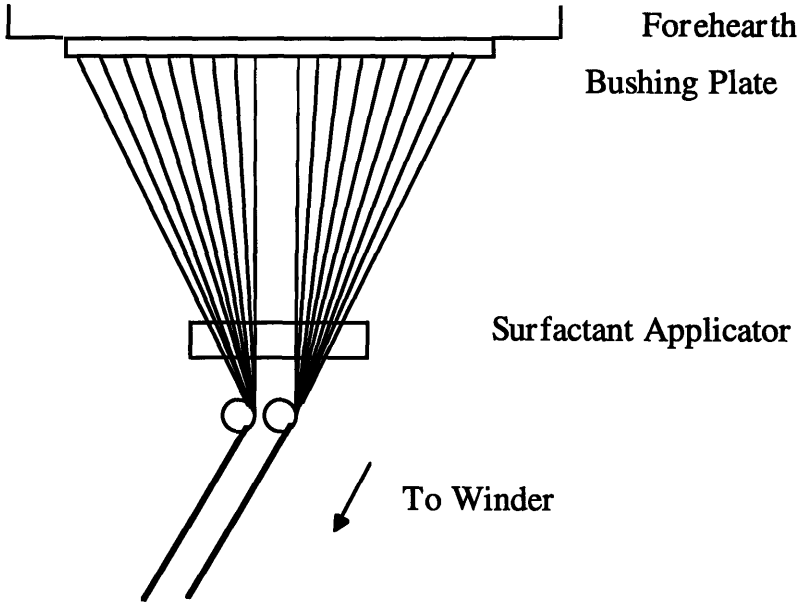

Fig. 1.1: A fiber glass forming position.

Much work has been done to better understand the fiber glass forming process. As will be discussed in Chapter 2, research has been done to model the thermal and velocity boundary layers of a single filament, though little experimental data has been obtained. These theoretical studies have gone on to estimate the cooling rates and times of a continuously drawn fiber. In addition, some theoretical work has been performed which

investigates the effects of forced convection on the cooling of the fibers, and research has also been done by Sweetland [15] to model the effects of spray cooling on the heat transfer rates. Little work, however, has gone towards obtaining experimental data on the temperatures and air speeds in the actual fiber forming environment. This is information which could be valuable in trying to validate and improve the numerous theoretical models that have been developed. Looking at the bigger picture, this will help the fiber glass industry better understand how varying its process parameters affects the physics of the fiber glass forming process More specifically, the data obtained should help in predicting the cooling rates and times of the fibers, given a set of operating conditions, or at the very least, draw correlations between the operating conditions and cooling rates and times of the fibers.

This paper goes on to explain in more detail the smaller-scale melter that was used to simulate a simplified production-scale fiber forming position. The apparatus was used in order to obtain experimental data for air temperatures and air velocities in the forming environment. The chapter includes, in addition to a detailed description of the apparatus, an explanation of the positioning systems used for the measurement devices. Following is a chapter on previously completed work on the cooling of glass fibers along with an example of an analysis aimed at showing some background fiber cooling theory. In addition, the analysis shows the relevance of air temperature and air velocity measurements to predicting cooling rates and times given a set of operating conditions. The next chapter of the paper describes the choice of measurement devices and the

considerations made while choosing them. The chapter describes a model that was developed in order to account for errors in air temperature measurements due to radiation from the bushing plate and heat loss from conduction through the thermocouple leads. Next is a chapter covering the experimental results obtained. This includes determining fiber diameters for a range of bushing temperatures and winder speeds, along with air temperature and air velocity data for a variety of those operating conditions. Additionally, the results sections compares raw temperature data to temperature data corrected by the model outline in the previous section. Following is a discussion on the results and how they can be interpreted and used to gain information about fiber cooling.

2. Previous Work on Glass Fiber Cooling

2.1 Summary of Previous Work

Much work has been done on boundary layer growth and heat transfer from moving continuous cylinders in a still fluid. Seband & Bond [14] and Kelly [9] developed an early theoretical prediction for the drag coefficient for a cylinder in steady, incompressible flow, and Glauert & Lighthill [6] further developed the analysis. Sakiadis [13] applied the technique used by Glauert & Lighthill to a continuous cylindrical surface, as opposed to the finite surface that was previously used;. His results paralleled those of Glauert & Lighthill but on average fall about 20% below their predictions.

Bourne & Dixon [4] used the von Kármán Polhausen integral method to solve the boundary layer equations, in conjunction with an equation governing the rate of supply of heat to the fluid from the fiber. They used an averaging method to account for the variation of temperature, and hence, fluid properties in the forming environment. Bourne & Dixon's theoretical results compare very well experimental results by Alderson et al.

[1] and Arridge & Prior [3]. Chida & Katto [5] improved Bourne & Dixon's model to include the effects of radial heat conduction within the fibers. Those effects, they found, tend to be negligible for conditions typical of glass fibers. In addition, Chida & Katto developed a set of scaling parameters that collapsed the experiments of Alderson et al. and Arridge & Prior. Kang et al. [8] performed experiments on large-diameter aluminum cylinders that were drawn through air and water. These results generally agreed with the scaled results of Chida & Katto. Madison & McMillan [9] also performed fiber cooling experiments which had results in agreement with those of Arridge & Prior.

2.2 Sample Theoretical Model

The main goal of this study was to find data that provides insight into better understanding the fiber glass forming process, particularly the cooling of glass fibers. The air temperature and air velocity data obtained in this yield valuable information pertaining to both the momentum and temperature boundary layers. As outlined later in this chapter, this information can be directly related to the cooling rates and cooling times of continuous strand fibers, as adopted from an article by Glicksman [7].

As touched on in the previous section, an analytical prediction of the drag coefficient for a cylinder in steady incompressible flow has been developed by Seban & Bond, Kelly, and Glauert & Lighthill. The model assumed laminar flow and neglected effects of the cylinder's leading edge. Seban & Bond and Kelly expanded the stream function as a series of the function ($\nu x/U_\infty r^2$), which is proportional to the ratio of the flat plate

boundary layer thickness to the radius of the cylinder; however, this is only valid for low values of this function.

Glauert & Lighthill improved on the work of Seban & Bond and Kelly by using the von Kármán Polhausen integral technique to find results for large values of the function ($\nu x/U_\infty r^2$). Their results indicate that the non-dimensionalised local shear stress, $\tau_w 2\pi r/\nu U_\infty$, and the non-dimensionalised momentum defect area, $\theta/\pi r^2$, are functions of the variable ($\nu x/U_\infty r^2$). Sakiadis further improved on the model by applying Glauert & Lighthill's technique to a continuous cylindrical surface. This situation occurs, for example, when winding continuous strand fiber glass.

Assuming no pressure gradients and negligible viscous dissipation, one obtains the following boundary layer equations:

$$\frac{\partial \upsilon_x}{\partial} + \upsilon_r \frac{\partial \upsilon_x}{\partial r} + r_x \frac{\partial \upsilon_x}{\partial x} = \nu\left(\frac{\partial^2 \upsilon_x}{\partial r^2} + \frac{1}{r}\frac{\partial \upsilon_x}{\partial r}\right). \tag{2.2.1}$$

where υ is the air velocity, t is time, r is the fiber radius, ν is kinematic viscosity of the air, and the subscripts x and r indicate axial and radial components, respectively. The boundary conditions for the momentum equation are:

$$\upsilon_x = 0, \upsilon_r = 0, \text{at } r = r_0, \qquad (2.2.2)$$
$$\upsilon_x \to U_\infty \text{ as } r \to \infty.$$

where r_0 is the fiber radius, and U_∞ is the velocity of the air far from the fiber. The energy equation is as follows:

$$\frac{\partial T}{\partial t} + \upsilon_r \frac{\partial T}{\partial r} + \upsilon_x \frac{\partial T}{\partial x} = \frac{k}{\rho c_p}\left(\frac{\partial^2 T}{\partial r^2} + \frac{1}{r}\frac{\partial T}{\partial r}\right). \qquad (2.2.3)$$

where T is air temperature, and k, ρ, and c_p are the thermal conductivity, density, and specific heat, respectively, of the air. The boundary conditions of the energy equation are:

$$T = T_0 \text{ at } r = r_0,$$
$$T \to T_\infty \text{ as } r \to \infty. \qquad (2.2.4)$$

where T_0 is the fiber temperature at the fiber surface, and T_∞ is the temperature of the air far from the fiber. These equations can be non-dimensionalized by defining the following non-dimensional variables:

$$\bar{v}_x = \frac{\upsilon_x}{U_\infty}, \bar{v}_r = \frac{\upsilon_r}{U_\infty}, \bar{t} = \frac{tU_\infty}{r_0}, \bar{r} = \frac{r}{r_0}, \bar{x} = \frac{x}{r_0}, \text{ and } \bar{T} = \frac{T - T_0}{T_\infty - T}. \qquad (2.2.5)$$

where x is the axial length from the leading edge of the fiber, and $\bar{v}_x, \bar{v}_r, \bar{t}, \bar{r}, \bar{x}$, and $\bar{T}$ are the non-dimensional axial velocity component, radial velocity component, time, fiber radius, axial length from the leading edge of the fiber, and temperature, respectively. Using these non-dimensional variables, the boundary layer equations can be re-written.

$$\frac{\partial \bar{v}_x}{\partial \bar{t}} + \bar{v}_x \frac{\partial \bar{v}_x}{\partial \bar{r}} + \bar{v}_x \frac{\partial \bar{r}_x}{\partial \bar{x}} = \frac{1}{(\mathrm{Re})_r}\left(\frac{\partial^2 \bar{v}_x}{\partial \bar{r}^2} + \frac{1}{\bar{r}} \frac{\partial \bar{r}_x}{\partial \bar{r}} \right). \tag{2.2.6}$$

with

$$(\mathrm{Re})_r = \frac{v_x r}{\nu}. \tag{2.2.7}$$

where $(\mathrm{Re})_r$ is the Reynolds number based on fiber radius. The boundary conditions for the new momentum equation are:

$$\bar{v}_x = 0, \bar{v}_r = 0, r = 1; \bar{v}_x \to 1 \text{ as } r \to \infty. \tag{2.2.8}$$

The new energy equation is:

$$\frac{\partial \bar{T}}{\partial \bar{t}} + \bar{v}_r \frac{\partial \bar{T}}{\partial \bar{r}} + \bar{v}_x \frac{\partial \bar{T}}{\partial \bar{x}} = \frac{1}{(\mathrm{Re})_r} \frac{1}{(\mathrm{Pr})} \left(\frac{\partial^2 \bar{T}}{\partial \bar{r}^2} + \frac{1}{r} \frac{\partial \bar{T}}{\partial \bar{r}} \right). \tag{2.2.9}$$

where Pr is the Prandtl number. The boundary conditions of equation 2.2.9 are:

$$\bar{T} = 0 \text{ at } \bar{r} = 1; \bar{T} \to 1 \text{ as } \bar{r} \to \infty. \tag{2.2.10}$$

The momentum and energy equations take exactly the same form when the Prandtl number is equal to one, and the solution to equation 2.2.9 is:

$$\bar{T}(\bar{r}, \bar{x}, \bar{t}) = \bar{v}_x(\bar{r}, \bar{x}, \bar{t}) \tag{2.2.11}$$

Because time-dependent terms were included in the equations, equation 2.2.11 holds true for both laminar and turbulent flow. Therefore:

$$(Nu)_D = \frac{hD}{k} = \frac{D}{k} \frac{(q/A)_{r_0}}{(T_0 - T_\infty)} = -\frac{D}{k} \frac{k\left(\frac{\partial T}{\partial r}\right)_{r_0}}{(T - T_\infty)} = 2\left(\frac{\partial \bar{T}}{\partial \bar{r}}\right)_{r=1}. \tag{2.2.12}$$

where $(Nu)_D$ is the local Nusselt number for a cylinder, D is the fiber diameter, h is the local film coefficient of heat transfer, and q/A is the heat transfer rate per unit area. From equation 2.2.11, if Pr = 1, then:

$$\left(\frac{\partial \bar{T}}{\partial \bar{r}}\right)_{\bar{r}=1} = \left(\frac{\partial \bar{v}_x}{\partial \bar{r}}\right)_{\bar{r}=1}. \tag{2.2.13}$$

So,

$$(Nu)_D = 2\left(\frac{\partial v_x}{\partial \bar{r}}\right)_{\bar{r}=1} = 2\frac{r_0}{U_\infty}\left(\frac{\partial v_x}{\partial r}\right)_{r=0} = \frac{\tau_w D}{U_\infty \mu} = \frac{1}{2}C_f(\mathrm{Re})_D. \tag{2.2.14}$$

where τ_w is the local shear stress at the fiber wall, μ is the viscosity of the air, C_f is the local drag coefficient, and $(\mathrm{Re})_D$ is the Reynolds number based on the diameter of the fiber. Averaging the Nusselt number over the length of the fiber gives the following result:

$$\left(\overline{Nu}\right)_D = \int_0^L \frac{(Nu)_D\,dx}{L} = \frac{1}{2}\overline{C}_f(\mathrm{Re})_D = \frac{\theta}{\pi r^2}\left(\frac{\nu L}{U_\infty r^2}\right)^{-1}. \tag{2.2.15}$$

where $\left(\overline{Nu}\right)_D$ is the average Nusselt number, L is the length of the fiber, $\overline{C}_f$ is the average drag coefficient, and θ is the momentum-defect area. The results for shear stress from Glauert & Lighthill can be combined with the Reynolds analogy to yield predictions for the local Nusselt numbers. As shown by Glicksman [7], Plotting predictions and approximating the curves gives equation 2.2.16, which is valid for values of $(\nu x/U_\infty r^2)$ greater that 10:

$$(Nu)_D = \frac{4\cdot 3}{\ln\left(\frac{4\nu x}{U_\infty r^2}\right)} - \frac{12\cdot 9}{\left[\ln\left(\frac{4\nu x}{U_\infty r^2}\right)\right]^3}. \tag{2.2.16}$$

And equation 2.2.17 is the result averaged over the length of the fiber, as stated by Glicksman [7]:

$$(\overline{Nu})_D = \frac{4\cdot 3}{\ln\left(\frac{4\nu L}{U_\infty r^2}\right)} + \frac{4\cdot 3}{\left[\ln\left(\frac{4\nu L}{U_\infty r^2}\right)\right]^2} - \frac{4\cdot 3}{\left[\ln\left(\frac{4\nu L}{U_\infty r^2}\right)\right]^3}. \tag{2.2.17}$$

The equation for the cooling rate of a glass fiber may be obtained by using a moving control volume that follows a single element of glass. Assuming a negligible temperature difference from the centerline of the fiber to the surface of the fiber, the energy equation for an element of glass may be written:

$$\frac{\partial}{\partial \tau}\left(\rho_g \pi r^2 c_{p_g} T\right) = -h(2\pi r)(T - T_\infty). \tag{2.2.18}$$

where ρ_g and c_{p_g} are the density and specific heat of the glass, respectively. Further assuming that the radius, density, and specific heat of the glass fiber are constant, equation 2.2.19 results:

$$\frac{1}{(T - T_\infty)}\frac{\partial T}{\partial \tau} = \frac{2h}{\rho_g r c_{p_g}} = -\frac{k(Nu)_D}{\rho_g r^2 c_{p_g}}. \tag{2.2.19}$$

As stated in equation 2.2.14:

$$(Nu)_D = \frac{h2r}{k}. \tag{2.2.20}$$

Integrating equation 2.2.19 yields:

$$\frac{T - T_\infty}{T_0 - T_\infty} = \exp\left[-\frac{k(Nu)_D t}{\rho_g r^2 c_{p_g}} \right]. \tag{2.2.21}$$

Rewriting equation 2.21 gives:

$$\frac{kt}{\rho_g c_{p_g} r^2} = -\frac{1}{(Nu)_D} \ln\left(\frac{T - T_\infty}{T_0 - T_\infty} \right). \tag{2.2.22}$$

Assuming a laminar boundary layer and that the fiber has reached its final radius, Glicksman [7] shows that equations 2.2.17 and 2.2.22 can be combined to give the following prediction for the cooling time of a glass fiber:

$$t = \frac{\rho_g c_{p_g} r^2}{k} \frac{\ln\left(\frac{4\nu x}{U_\infty r^2} \right)}{4 \cdot 3} \ln\left(\frac{T - T_\infty}{T_0 - T_\infty} \right). \tag{2.2.23}$$

It is evident from the model outlined in this section that air temperature and air velocity data are essential for understanding the cooling of glass fibers as they are drawn. Unfortunately, it is difficult to accurately predict cooling times without accurate data for fiber surface temperature, but the velocity and temperature data found in this study will nonetheless provide valuable information.

3. Apparatus

3.1 The Marble Melt

The apparatus that was used to simulate a production level fiber forming position was a smaller scale marble melt position. The apparatus, shown in figure 3.1.1 consists of an isolated chamber in which glass marbles are melted. The molten glass is pulled through a bushing plate that is much smaller than those used in production and therefore has a smaller number of orifices, or bushing tips. The bushing well, plate, and tips are made of a platinum-rhodium alloy and are contained in and supported by a larger box filled with refractory cement. As in production, the resulting filaments pass over a surfactant applicator which binds the filaments together into a single fiber. A major difference, however, is that there are no water sprays or conditioned air flows used on this position. Though the absence of those components of the forming process makes the simulated process slightly different from the actual process used in production, it eliminates a large amount of variability and helps in making it possible to record consistent temperature and air speed measurements in the forming environment. Furthermore, due to the smaller

scale of the simulated process, the water sprays and conditioned air flows are non-essential in making the process work. That is not the case for the larger bushings used in production.

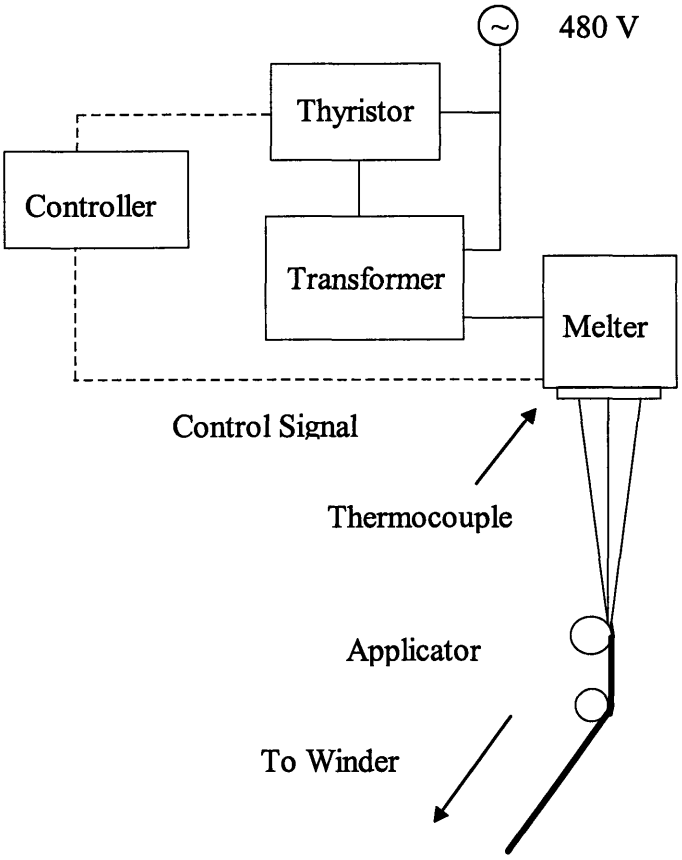

Fig. 3.1.1: The marble melt position.

The specifications of the marble melt apparatus used in this study are quite important for understanding the air flows in the forming environment. The bushing plate, located at the bottom of this chamber, is much smaller than the ones used in production. The bushing plate measures 3.1 cm by 3.1 cm and has nine tips arranged in a square grid in the center of the bushing plate. Adjacent tips are separated by a distance of 0.37 cm from center to

center. The tips measure 0.32 cm in length, 0.20 cm in outer diameter and 0.10 cm in inner diameter. The bushings sits 2.3 m above the floor, 2.0 m from the wall on the right-hand side, 7.0 m from the wall on the left-hand side, 5.0 m from the wall in front and 2.5 m from the wall in the back. A diagram of the bushing is shown in figure 3.1.2:

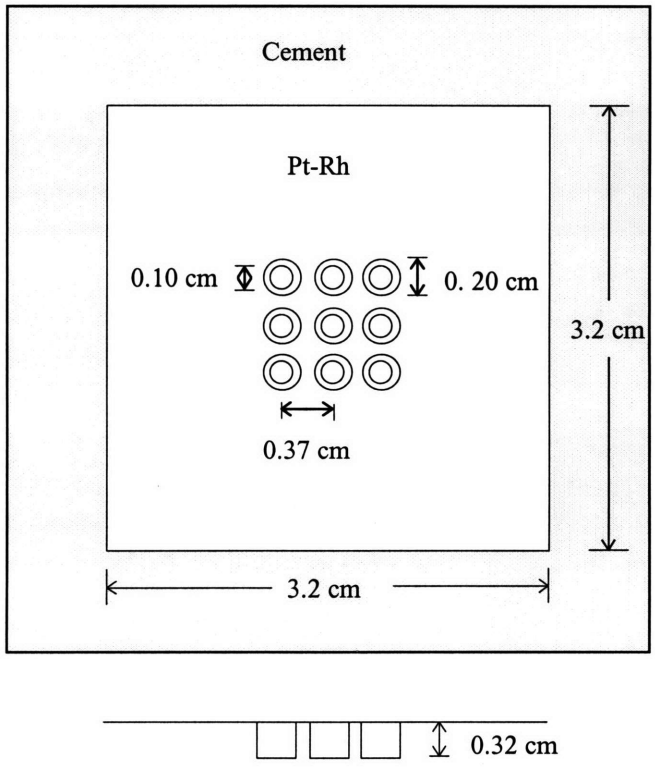

Fig. 3.1.2: Dimensions of bushing plate.

The bushing is electrically heated through a single phase 24 kVA transformer with a primary voltage of 480 VAC. When the bushing is at normal running temperature the secondary voltage is approximately 0.78 VAC at about 60 A. Due to the high degree of

power inherent to this system, the entire apparatus is cooled by a series of water lines. The power supplied to the bushing is regulated by a TCS Bushing Controller and a Eurotherm Thyristor, model number 463. The controller tracks the bushing temperature through the use of a type R thermocouple embedded in the bushing. This information is compared to the set point temperature entered into the controller by the user, and adjustments are made to the power in order to keep the bushing heated to the desired temperature. Typical temperatures at which the bushing plate was set were between 1477 K (2200 °F) and 1533 K (2300 °F).

The glass used in the melter was a standard composition of E-glass. Typically, approximately ten or twelve glass marbles were fed into the melter at the beginning of a set of trials, which translates to an initial head of approximately 8-10 cm of glass. In order for the fibers to be pulled, however, additional air pressure needed to be added on top of the molten glass. The necessary head varied with the level of glass in the melter and with the operating conditions, but generally was on the order of 1-2 psi.

At the time that the trials were run, a pressure control system had not been implemented yet, so all pressure control was done manually. A winder speed control system, however, was in use to insure that the fibers were drawn at constant rates. Details on both of these control systems is discussed by Ansberg [2].

3.2 The Three- Dimensional Traverse

In order to position the necessary measurement instruments around the forming environment in a precise manner it was necessary to develop a traverse system. The system was developed from a commercial two-dimensional positioning table. The device, which was designed to be a milling attachment to a drill press, has a travel distance of nine inches in either dimension. The table is adjusted using hand cranks, which position the table in both directions. Position can be adjusted to within approximately 0.03 cm in either direction; This uncertainty is mainly due to backlash in the screws.

It was necessary, however, to create a third degree of freedom in order to easily and precisely position the measurements in space, rather than in a single plane. The first generation of this was constructed by mounting the positioning table to a set of roller bearings. A pair of tracks was then mounted to the marble melt position, and the positioning table was hung securely from the tracks by the roller bearings. It was then possible for the positioning table to slide smoothly in the third dimension over a total distance of twenty-four inches.

A break system was added so that once the traverse was in its desired position, it would no longer move. The break system is simply two screws that, when turned, force a small

piece of metal into either rail, providing enough frictional force to prevent the unit from being accidentally moved. Figure 3.2.1 illustrates the entire system.

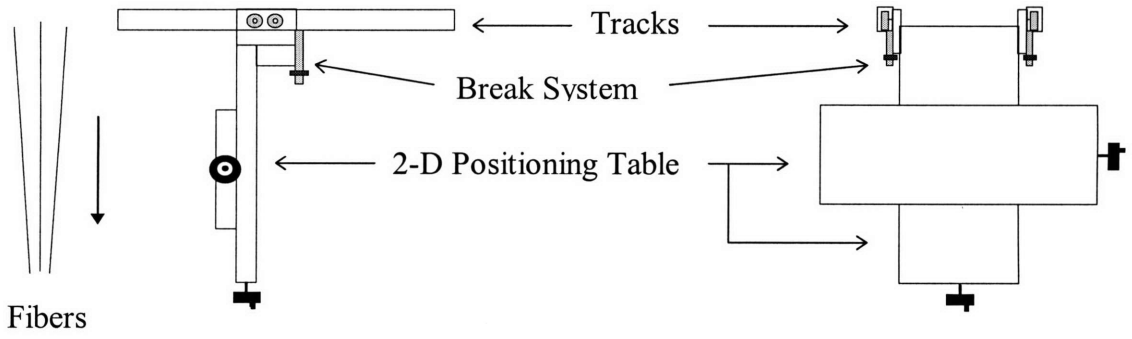

Fig. 3.2.1: The original three-dimensional traverse system.

While this method worked reasonably well, it did not provide adequate positioning precision. A second generation of this traverse involved mounting the original two-dimensional positioning table to a similar one-dimensional positioning table. This method proved to provide a significantly higher level of precision in the positioning of the measurement instruments. Figure 3.2.2 shows the second and final generation of the traverse:

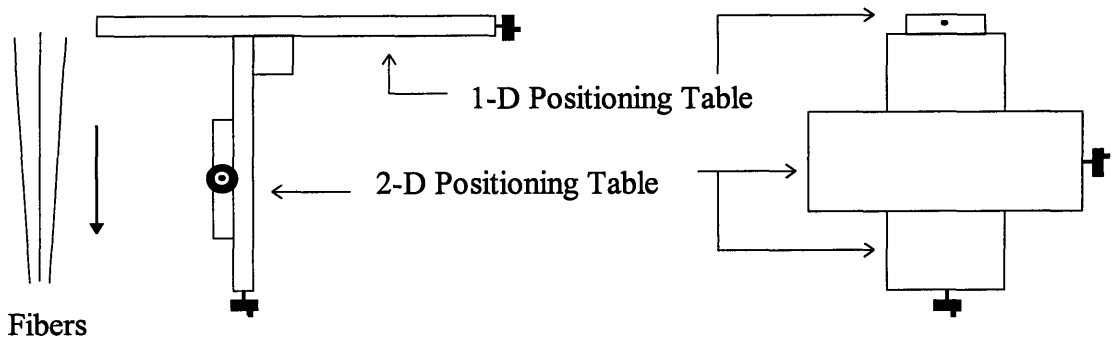

Fig. 3.2.2: Final generation of the three-dimensional traverse.

3.3 Data Acquisition

3.3.1 Introduction

To facilitate in recording data, a data acquisition system was set up. The computer used for the data acquisition was An AcerPower Flex4000. A National Instruments board, PC-4350, was installed and was used in conjunction with a National Instruments terminal block, TBX-68T. Virtual Bench 2.2 was the software used to log the temperature and velocity data. K-type thermocouples were used for the temperature measurements, and a pitot tube was used for the velocity measurements. The thermocouples were connected directly to the terminal block, while the pitot tube was first hooked up to a pressure transducer, which was then hooked up to the terminal block.

3.3.2 Hardware

The AcerPower Flex 4000 has a MMX Pentium chip running at 233 MHz. The computer has 32 MB and a 512 KB level 2 cache. The operating system of choice was Windows NT 4.0.

The PC-4350 is designed specifically for temperature measurements and for low-frequency analog signals within ±15V. The PC-4350 has an accuracy of approximately ±0.7 °C for the temperature range considered in this study. In addition, the it has an auto-zero feature as well as cold-junction compensation and open-thermocouple detection. The PC-4350 has 16 differential analog inputs or 14 thermocouple inputs and has 24-bit ADC resolution. The device has three reading rates-10, 50, and 60 readings per second in single channel acquisition mode and 2.8, 8.8, and 9.7 readings per second in multiple channel acquisition mode. Digital filters reject 50, 60, and 400 Hz noise, based on the reading rate. The input circuitry delivers ±42 V overvoltage protection and per-channel lowpass antialiasing filters. Software-selectable ground-referencing on a channel-by-channel basis is also available.

The TBX-68T is designed specifically for use with the PC-4350. This 68-pin, DIN-rail mountable terminal block provides screw-terminals for 14 unconditioned temperature or voltage signals as well as for the excitation and digital lines. The TBX-68T has an isothermal design, a plastic cover that minimizes temperature gradients across the

terminal block, a cold-junction compensation sensor on channel 0 and auto-zeroing circuitry on channel 1.

3.3.3 Software

The software of choice for the data acquisition was National Instruments' VirtualBench Version 2.1.1 This suite of software was chosen because of its intended compatibility with the PC-4350. This software package includes the VirtualBench-Logger program, a multichannel data logger for recording and displaying low-frequency signals (e.g. temperature, pressure, and voltage). The software operates as a soft front panel that controls the PC-4350 with no required programming. All hardware features of the PC-4350 are accessible by the software.

The VirtualBench-Logger wrote all of the data to tab-delimited .log files. These files were easily opened and manipulated using Microsoft Excel. For the temperature data, the VirtualBench-Logger was able to compute a temperature based on the input voltage and the settings for that channel. The temperatures were recorded directly into the aforementioned files. The velocity measurements were recorded in terms of voltage. The pressure difference from the pitot tube was the input for the pressure transducer, which then, based on the input, output a voltage that was recorded by the VirtualBench-Logger. Velocities then needed to be calculated manually, based on the specifications of the pressure transducer along with the properties of the air at the point in space of the measurement.

3.3.4 Measurement Instruments

The temperature measurements were made using a fine-gauged, unsheathed K-type thermocouple from Omega. The leads, made of Chromel and Alumel were each 0.13 mm in diameter, and the thermocouple bead was 0.30 mm in diameter.

The pitot tube was custom made by Vita Needle, Co. The tube is made from stainless steel, with an inner diameter of 1.2 mm, and an outer diameter of 1.8 mm. The tube was connected to a pressure transducer using 0.636 cm OD PVC tubing. The pressure transducer was a made by Setra, model number 264. The transducer required an excitation voltage of 12-28 V DC, and had an output range of 0-5 V DC. This corresponds to ±0.254 cm water column. This information, along with information about the air densities at the particular points in space, was used to calculate air velocities from output voltages.

Chapter 4 explains in-depth the method of selection of the measurement instruments.

4. Instrumentation

4.1 Air Temperature Measurements

4.1.1 Introduction

The major challenges in finding the best instrumentation for taking air temperature measurements was eliminating measurement error due to conduction and radiation, as well as obtaining adequate spatial resolution in the measurements. The following section details the process of instrumentation selection for air temperature measurements.

4.1.2 Early Instrumentation and Modeling

The earliest measurements were taken using a medium-gauge sheathed thermocouple. Concerns arose regarding the transfer of heat into the thermocouple junction through radiation from the bushing plate. This was undesirable because the temperature measurements that were desired were the air temperatures in the fiber glass forming environment. The radiation from the bushing plate heats the thermocouple junction

directly, potentially causing it to reach a temperature much greater than that of the surrounding air. The other major concern involved heat loss via conduction through the thermocouple leads.

As a means of accounting for the error caused, Equation 4.1.2.1 was developed in order to model the heat transfer to and from the thermocouple junction:

$$mc_p \frac{dT}{dt} = q_{rad}\varepsilon A_{tc} + hA_{tc}(T_{air} - T) + (k_{chromel} + k_{alumel})A_{lead}\frac{T - T_\infty}{\Delta x}. \qquad (4.1.2.1)$$

where m is the mass of the thermocouple junction, c_p is its specific heat; T is the measured temperature; t is time; q_{rad} is the radiative heat flux, h is the heat transfer coefficient; ε is the emissivity of the bushing plate; A_{tc} is the surface area of the thermocouple bead; T_{air} is the air temperature; $k_{chromel}$ is the thermal conductivity of the chromel thermocouple lead; k_{alumel} is the thermal conductivity of the alumel thermocouple lead; A_{lead} is the cross sectional area of one of the leads; T_∞ is the ambient temperature a fixed distance down the length of the thermocouple leads; and Δx is that distance.

Equation 4.1.2.1 contains three unknowns, T_{air}, q_{rad}, and h. These are values that cannot be looked up in a table or directly measured. In order to calculate the unknowns, a system of three equations would need to be used. A way of accomplishing that would be to take Equation 4.1.2.1 and use three different values for A_{tc}. More simply put, monitor the temperature T with three different sized thermocouples.

This approximation method was applied by creating a probe consisting of a thin ceramic-alumina cylinder with four holes running through the length of the cylinder. The three different sized thermocouples were placed in separate holes within the cylinder, with their respective junctions exposed at the end of the cylinder. A fourth thermocouple was placed within the cylinder to detect the ambient temperature at a point a fixed distance down the length of the other thermocouple leads. Figure 4.1.2.1 illustrates the probe.

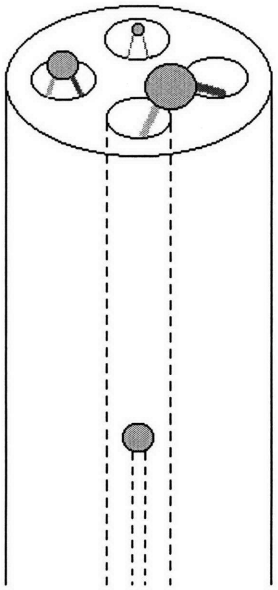

Fig. 4.1.2.1: Close up view of the three-thermocouple temperature probe

A data acquisition program kept track of the temperatures for periods of one minute, noting the beginning and final temperatures. Though conceptually a good idea, there were definite problems with the model. Extensive measurements were made using this probe, but data reduction using equation 4.1.2.2 proved to be intractable. Programs such

as Matlab and Maple had difficulties dealing with the complexity of this transient system. Furthermore, contrary to what was assumed, the heat transfer coefficient, h, in actuality was not the same for each of the thermocouples. These factors contributed to the need to find a different means of measuring or calculating air temperature.

4.1.3 Instrumentation and Modeling Improvements

Some simplifications to the model were made, the major one being converting equation 4.1.2.1 to a steady state equation. Instead of tracking temperatures over time, it would only be necessary to observe the steady state temperatures of each of the thermocouples. In addition the problem with heat transfer coefficient, h, was minimized. The following relationship was used by Mills [11] to account for differences in h from thermocouple to thermocouple:

$$h = 2\frac{k_{air}}{D_{tc}}. \tag{4.1.3.1}$$

where k_{air} is the thermal conductivity of the air and D_{tc} is the diameter of the thermocouple bead. Equation 4.1.3.1 is based on the fact that the Nusselt number for small spheres is approximately equal to 2. Substituting the new expression for h into equation 4.1.2.1 and removing the transient term yields equation 4.1.3.2:

$$0 = q_{rad}\varepsilon A_{tc} + 2\pi k_{air} D_{tc}(T_{air} - T) + (k_{chromel} + k_{alumel})A_{lead}\frac{T - T_{\infty}}{\Delta x}. \tag{4.1.3.2}$$

The model is now a pair of steady state equations with two unknowns. This system is much easier for programs such as Matlab and Maple to handle. The results obtained from this revised model, however, were somewhat unreliable. One reason is that the transfer of heat to the ceramic-alumina sheath was neglected because of the enormous complexity it would have added to the model. In addition, three thermocouples were being used to measure temperatures at the same point in space. Since it is impossible for three objects to occupy the same point in space, the three thermocouples, though close together, were actually measuring temperatures at three different points in the forming environment, where temperature gradients can be quite large at times.

4.1.4 More Instrumentation and Modeling Improvements

Despite all of the effort put into developing the previous models and measurement instruments, it was decided that there was still a better means of taking measurements and modeling the system. By using a very fine gauge (0.013 cm) exposed junction thermocouple, conductive heat loss though the leads would be minimized and the thermocouple would respond quickly to changes in temperature in the forming environment, thus reducing the time needed to obtain steady state measurements. Furthermore, the spatial resolution of such a fine gauge thermocouple makes it a desirable option, especially for taking measurements between individual fibers as they are pulled through the bushing plate. The main disadvantages to the fine gauge exposed junction thermocouple are its susceptibility to corrosion and its fragility. It would be ideal to use

an even finer gauge thermocouple than the one that was decided upon; however, something much finer would not be able to withstand the constant high temperatures to which it would need to be exposed.

Corrections still needed to be me made that could account for errors in temperature measurements caused by radiation from the bushing plate and from conduction through the leads. An improved steady state heat balance was developed to account for this. The thermocouple bead was modeled as a sphere, and the leads were modeled as a single cylindrical fin for the purpose of determining the conduction through the leads. As was the case in practice, the orientation of the fin in the model was horizontal, or parallel to the bushing plate. In addition, an equation for the view factor from the thermocouple to the bushing plate was determined in order to find the approximate radiation heat flux to the bead and the wire. The horizontal orientation of the thermocouple along with its small size relative to the size of the bushing plate made it possible to approximate the radiative heat flux as a constant value, i.e., the radiative heat flux did not vary along that length of the thermocouple in which the heat conduction occurs. This greatly simplified the modeling of conductive losses. Equation 4.1.4.1 was the final model used to correct temperature readings for radiation and conduction:

$$T - T_{\infty} = \frac{\frac{\pi}{2} D_b{}^2 + \left(\frac{\sqrt{\bar{h}_w P k_w A_c}}{2\bar{h}_w} \right)}{\pi \bar{h}_b \left(D_b{}^2 - \frac{1}{4} D_w{}^2 \right) + \sqrt{\bar{h}_w P k_w A_c}} (\alpha q_{rad}). \qquad (4.1.4.1)$$

where T is the measured temperature; T_∞ is the corrected value for the air temperature; qrad is the approximate radiative heat flux to the thermocouple bead and wire, based on a view factor calculation; α is the absorbtivity of the bead and wire; $\bar{h}_w$, k_w, P, A_c, and D_w are the heat transfer coefficient, thermal conductivity, effective perimeter, effective cross sectional area, and effective diameter, of the thermocouple wires, respectively; and D_b is the diameter of the thermocouple bead.

A more comprehensive equation to better approximate the heat transfer coefficient of the thermocouple bead in moving air was found and is shown by Equation 4.1.4.2 below:

$$\bar{h}_b = \left(\frac{k_a}{D_b}\right)\left\{2 + \frac{0.589\mathrm{Ra}_D^{1/4}}{\left[1+(0.559/\mathrm{Pr})^{9/16}\right]^{16/9}}\right\}. \qquad (4.1.4.2)$$

where k_a is the thermal conductivity of the air, Ra_D is the Rayleigh number based on diameter, and Pr is the Prandtl number. In addition, it was necessary to find and equation for the heat transfer coefficient of the thermocouple wire. This is shown by Equation 4.1.4.3 below:

$$\bar{h}_w = \left(\frac{k_a}{D_w}\right)\left\{0.36 + \frac{0.518\mathrm{Ra}_D^{1/4}}{\left[1+(0.559/\mathrm{Pr})^{9/16}\right]^{4/9}}\right\}. \qquad (4.1.4.3)$$

An outline of the entire derivation of the final model can be found in Appendix A.

4.2 Air Velocity Measurements

4.2.1 Introduction

The main challenge in measuring air flows in the fiber glass forming environment was finding an instrument small enough to be positioned within the fiber bundle and which has a measurement area that can be positioned close enough to a moving filament to detect the moving air entrained by that filament.

4.2.2 Early Instrumentation

The first attempts at measuring air flows within the forming environment were made using a pitot static tube. The pitot static tube uses Bernoulli's Equation for determining air velocities. The moving air passes through the tube, creating pressure at the other end. Surrounding the tube is an outer chamber that is used to measure the static pressure. The differences in these pressures is the final output, from which an air velocity can be calculated from equation 4.2.2.1, derived from Bernoulli's Equation:

$$V = \sqrt{\frac{2(\Delta p)}{\rho}}. \qquad (4.2.2.1)$$

where V is the calculated average vertical air velocity across the diameter of the pitot tube, ρ is the air density, a functon of air temperature, and Δp is the pressure difference sensed by the pressure transducer.

The main problem with the pitot static tube that was used originally was it's bulkiness. It was difficult to position the device close enough to a moving filament to pick up a response, and it was nearly impossible to position it between individual filaments. Improvements needed to be made.

4.2.3 Instrumentation Improvements

Instead of using a pitot-static tube, it was decided to use a pitot tube instead. The difference is that the pitot tube does not have the outer chamber used to measure the static air pressure. Instead the static air pressure is assumed to be the pressure felt at the open input of the pressure transducer. This arrangement is desirable because since there is no outer chamber surrounding the tube, the outside diameter of the tube is considerably smaller. Therefore, the opening in the tube may be positioned closer to the moving fibers, allowing the tube to feel more of the air entrained by the moving fibers.

One issue that needed to be addressed was the role of viscous effects in the pitot tube. Bernoulli's equation is based on inviscid flow, so a significant viscous effect around the tube would lead to error in the air velocity results. In order for viscous effects to be negligible, the following benchmark has been set: According to White [16], if the Reynolds number based on the inner diameter of the pitot tube is greater than 100, viscous effects may be ignored. This is shown by Equation 4.2.3.1 below:

$$\mathrm{Re}_d = \frac{Ud}{\nu} > 100. \qquad (4.2.3.1)$$

where Re_d is the Reynolds number based on diameter, U is the air velocity, d is the inner diameter of the pitot tube, and ν is the kinematic viscosity of air. As good fortune would have it, the lowest velocities that were measured in the present experiments resulted in Reynolds numbers of approximately 100. This indicates that the pitot tube being used was the ideal size for this application. A smaller tube would have yielded bad results because of viscous effects, while a larger tube would not have been able to be positioned as easily between the fibers, and it would have poorer spatial resolution.

5. Results

5.1 Introduction

The main goal of this study was to determine how varying operating conditions in the glass fiber forming process affects the air temperature and air velocity distributions in the fiber glass forming environment. Ultimately, this information would be used to draw correlations between those process parameters and the cooling rates of glass fibers.

Temperature and velocity data were taken as fiber glass was formed using the marble melt apparatus. The pitot tube and thermocouple were placed at various locations within the fiber bundle. The two process parameters that could be accurately controlled were fiber speed and bushing temperature. In controlling both fiber speed and bushing temperature, fiber diameter was also controlled since it is a function of those two parameters. Data was taken for fiber speeds of 12.2 m/s (40 ft/s), 15.3 m/s (50 ft/s), 18.3 m/s (60 ft/s), and 21.3 m/s (70 ft/s), at bushing temperatures of 1477 K (2200 °F), 1505 K (2250 °F), and 1533 K (2300 °F), with everything else held constant. Essentially, this can be looked at as pulling three different diameter fibers for each of the four different fiber speeds. The 56 K bushing

temperature range is small relative to the minimum bushing temperature used, 1477 K, which means the temperature of the glass exiting the bushing tips does not vary significantly over that range of bushing temperatures. This, of course, is assuming a linear relationship between bushing temperature and temperature of the exiting glass. However, the viscosity of the glass varies greatly; According to White [16], liquid viscosity decreases with temperature and is roughly exponential:

$$\mu \approx ae^{-bT}. \tag{5.1.1}$$

where μ is the glass viscosity, T is temperature, and a and b are constants. But a better fit is the empirical result that ln μ is quadratic in $1/T$, where T is absolute temperature. The following expression is that empirical result:

$$ln\frac{\mu}{\mu_0} \approx a + b\left(\frac{T_0}{T}\right) + c\left(\frac{T_0}{T}\right)^2. \tag{5.1.2}$$

where μ_0 and T_0 are the initial viscosity and temperature respectively, and c is another constant. Unfortunately, values for a, b, and c, for glass were unavailable; however, it can still be seen that while changing the bushing temperature does not greatly affect the temperature of the exiting glass, it does significantly affect the viscosity of the glass. As a result, higher bushing temperatures result in faster mass flow through the tips and consequently, larger diameter fibers.

This chapter will detail the experimental results obtained. The first section will discuss experimental findings on how winder speed and bushing temperature relate to the fiber diameter. The second section will show some of the raw temperature data compared with the corrected results obtained through he

use of the model discussed in chapter 4. Following that, air temperature profiles of the forming environment will be revealed for different fiber speeds and bushing temperatures. These results will then be related to fiber diameter. The following section will discuss findings about air velocities in the forming environment and how they relate to fiber speed and bushing temperature. Finally, relationships will be drawn between fiber diameters and the experimental air velocity results.

5.2 Fiber Diameter Results

Typically, glass fibers are drawn at rates varying between 3 m/s and 30 m/s. In production, different fiber speeds result in different fiber diameters. i.e., the faster the rate at which the fiber is drawn, the smaller the fiber diameter, assuming all other variables are held constant.

In addition, as detailed in the previous section, fiber diameter is also a function of bushing temperature. Increasing the temperature of the bushing increases the glass temperature, which, in turn, decreases the viscosity of the glass. Less viscous glass flows more easily out of the bushing tips, resulting in higher-diameter fibers.

For the purposes of this investigation, it was necessary to map the fiber diameters as a function of winder speed and bushing temperature for the nine-tip system. Bushing speeds ranging between 12.2 m/s (40 ft/s) and 21.3 m/s (70 ft/s) were used and temperatures between 1477 K (2200 °F) and 1533 K (2300 °F). Packages of fiber glass were pulled over known time intervals, and their masses were recorded. A package is simply a term used to describe any amount of continuous-strand fiber glass wound on to a spool. By keeping track of the mass flow rates, it was possible to determine the fiber

diameters for each set of boundary conditions tested. Figure 5.2.1 illustrates the results as a function of fiber speed:

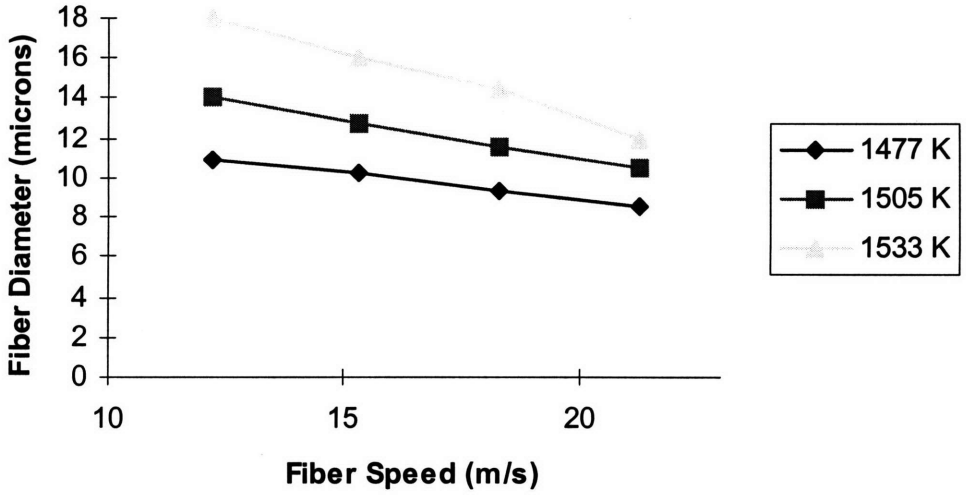

Fig. 5.2.1: Fiber diameter as a function of fiber speed. Data was taken using the nine-tip marble melt system. Fibers were drawn at 12.2 m/s, 15.3 m/s, 18.3 m/s, and 21.3 m/s. For each speed, bushing temperatures of 1477 K, 1505 K, and 1533 K were used.

It is apparent from figure 5.2.1 that the speed at which the fiber is drawn has a significant effect on the diameter of the fiber. On average, for a given bushing temperature, the data shows that a 75 % increase in fiber speed corresponds to about a 20 % change in fiber diameter. Figure 5.2.2 shows the same data as figure 5.2.1, but shows fiber diameter as a function of bushing temperature:

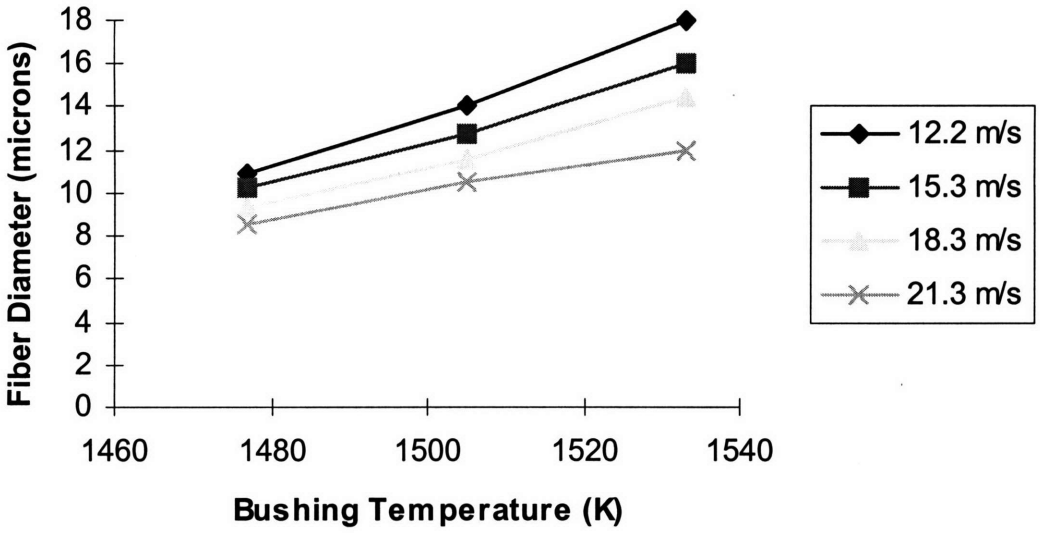

Fig. 5.2.2: Fiber diameter as a function of bushing temperature. This data is for the nine-tip system with bushing temperatures of 1477 K, 1505 K, and 1533 K. For each temperature, fiber speeds of 12.2 m/s, 15.3 m/s, 18.3 m/s, and 21.3 m/s were used

Figure 5.2.2 reveals that a mere 3.7 % increase in temperature results in an average increase in fiber diameter of approximately 50 %. This indicates that fiber diameter is much more sensitive to temperature than it is to fiber speed.

While using the marble melt apparatus, another element of difficulty is added to the control of fiber diameters. The level of glass in the bushing well is constantly decreasing, which results in a decreasing level of pressure above the bushing plate. If this issue is not addressed, the fiber diameter of a given package of glass will also decrease with time. In production, on the other hand, the glass level remains constant since new glass is constantly flowing down the forehearth above the bushing tips, resulting in a constant head, and hence, constant fiber diameters.

It is necessary to pressurize the bushing well in the marble melt apparatus because otherwise, the mass of glass above the bushing tips would be insufficient for drawing fibers. The best way of attempting to maintain a constant head in this apparatus is to slowly increase the level of added air pressure to the bushing well as the level of glass in the bushing well drops. By knowing the initial level of glass in the well, the initial air pressure being added, and the approximate length of time for the well to run out of glass, it is possible to maintain a roughly constant head over time. Ansberg [2] discusses an automated pressure control system that was under development at the time of this study. That system will greatly increase the accuracy and ease in maintaining a constant pressure over time at the bushing tips, and as a result, help in maintaining a constant fiber diameter.

5.3 Air Temperature Results

Obviously, by manipulating the winder speed, the speed at which the fibers are drawn changes. This should change the amount of air entrained by the fibers, which, in turn, should change the air velocity and air temperature distributions in and around the fiber bundle. Also, as the fiber thickness changes, so too should the air temperature and air velocity distributions. Among the more interesting areas to look at is the area between two individual filaments. The filaments that were used for this study were the front left and front middle filaments on the following nine-tip busing arrangement shown in Figure 5.3.1:

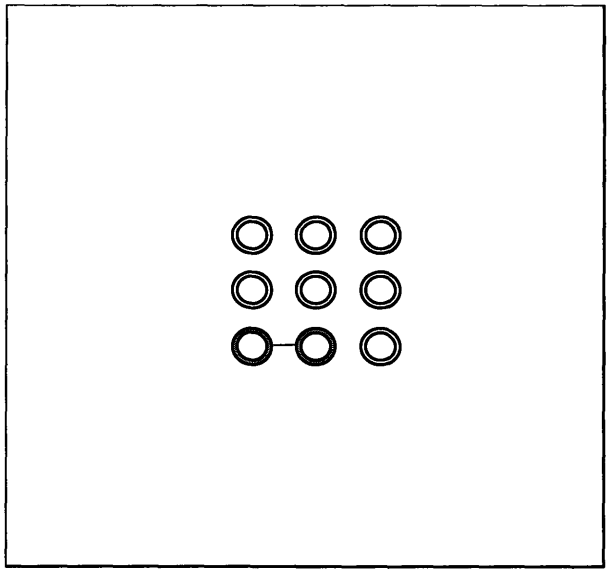

Fig. 5.3.1: Top View of Bushing Plate. The circles represent the bushing tips, the gray ones being the tips between which the temperature and velocity data was taken. The horizontal line between the two represents the exact location of the measurements.

Temperatures were recorded at a series of points between the two filaments at a number of winder speeds. The intent was to see how air temperatures change as the distance from the bushing plate increases as well as how air temperatures change as the horizontal position between the fibers changes. The first fiber speed that was used was 12.2 m/s, (40 ft/s). The bushing temperature was set at 1505 K, (2250 °F). Temperature data between the two filaments was taken at points of vertical distances between approximately 1 cm and 10 cm from the bushing plate. Points closer to the bushing plate than what is covered by that range would not yield useful results. In order for the model for temperature correction discussed in section 4.1.4 to work, air temperatures would need to be less than or equal to approximately 475 K because of assumptions made in the model about the heat transfer coefficients. Not only would that not have been the case for those points in space, based on preliminary data, but a

significant degree of air flow would not have had enough time or space to develop yet. At approximately 10 cm from the bushing plate is when the air temperatures begin to plateau.

Following are a few examples that compare the raw temperature data to the corrected temperature data. The corrected temperature data is indicative of a best estimate of the true air temperatures at the indicated points in space of the forming environment.

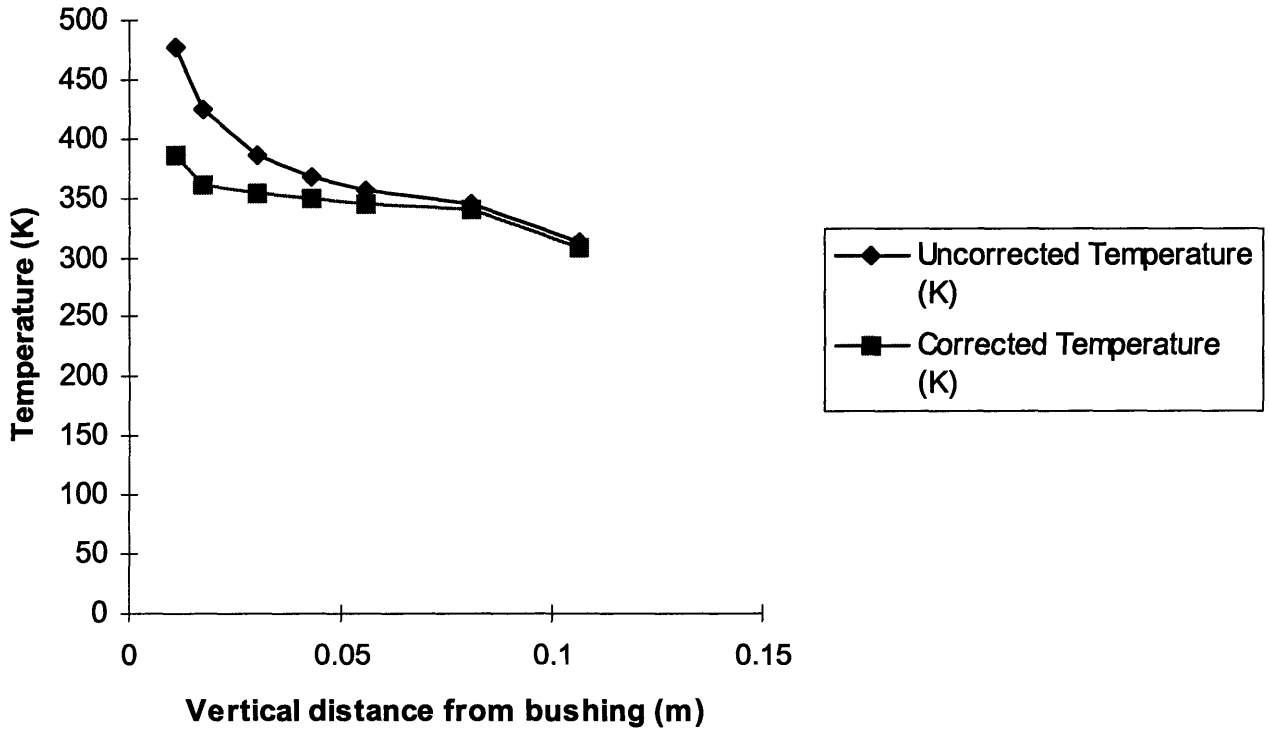

Fig. 5.3.2: Comparison of raw temperature data to the corrected temperature data as a function of vertical distance from the bushing plate. This data is for a nine-tip bushing with a fiber speed of 12.2 m/s, a bushing temperature of 1505 K, and a horizontal position located half way between the left-front and front-center fibers.

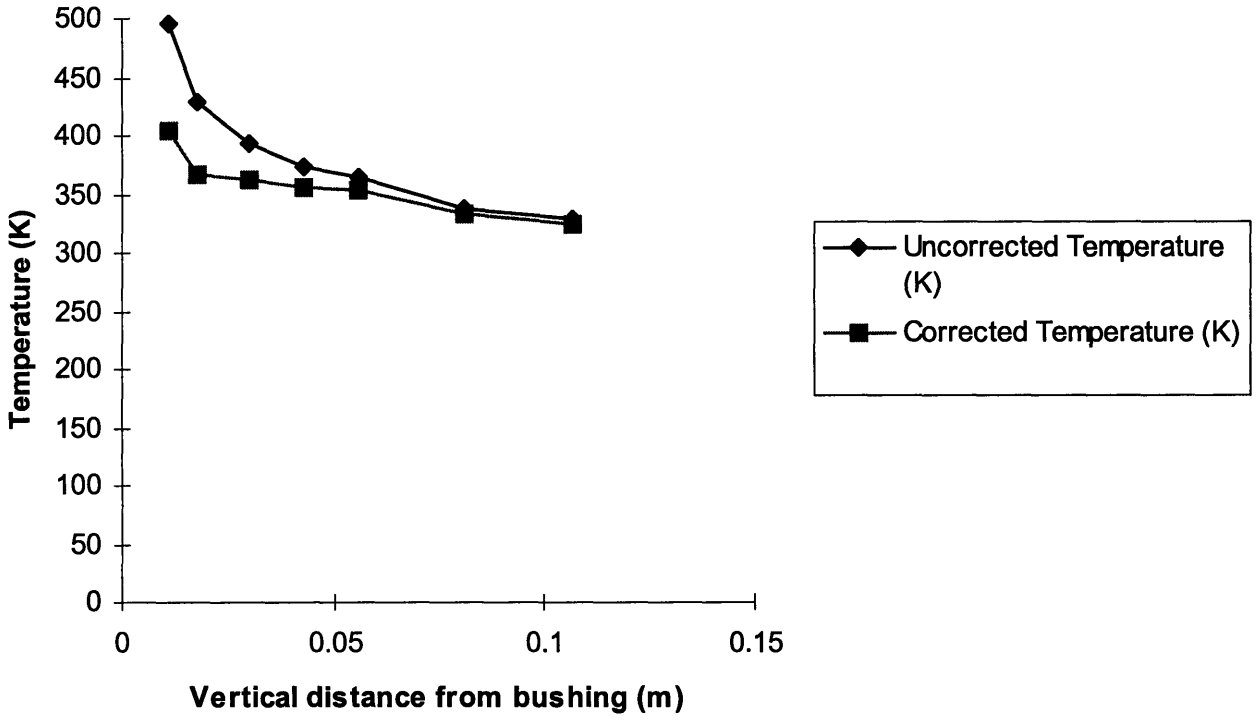

Fig. 5.3.3: Comparison of raw temperature data to the corrected temperature data as a function of vertical distance from the bushing plate. This data is for a nine-tip bushing with a fiber speed of 15.3 m/s, a bushing temperature of 1505 K, and a horizontal position located half way between the left-front and front-center fibers.

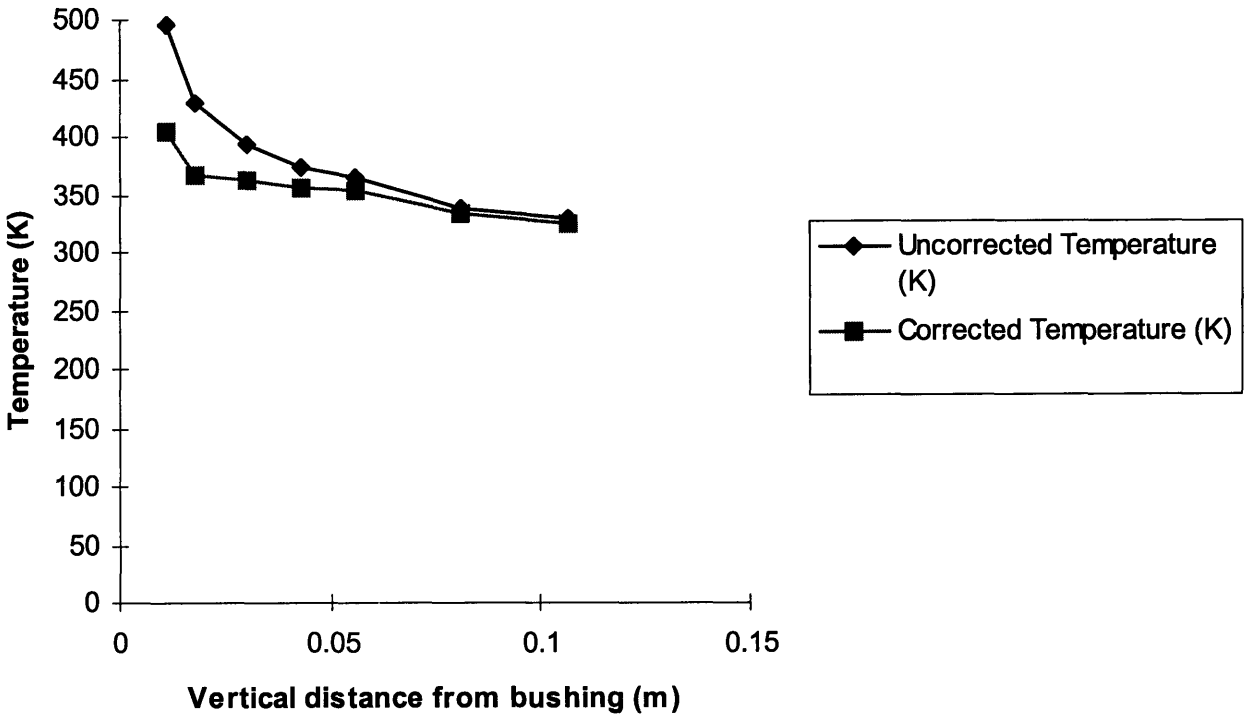

Fig. 5.3.4: Comparison of raw temperature data to the corrected temperature data as a function of vertical distance from the bushing plate. This data is for a nine-tip bushing with a fiber speed of 18.3 m/s, a bushing temperature of 1505 K, and a horizontal position located half way between the left-front and front-center fibers.

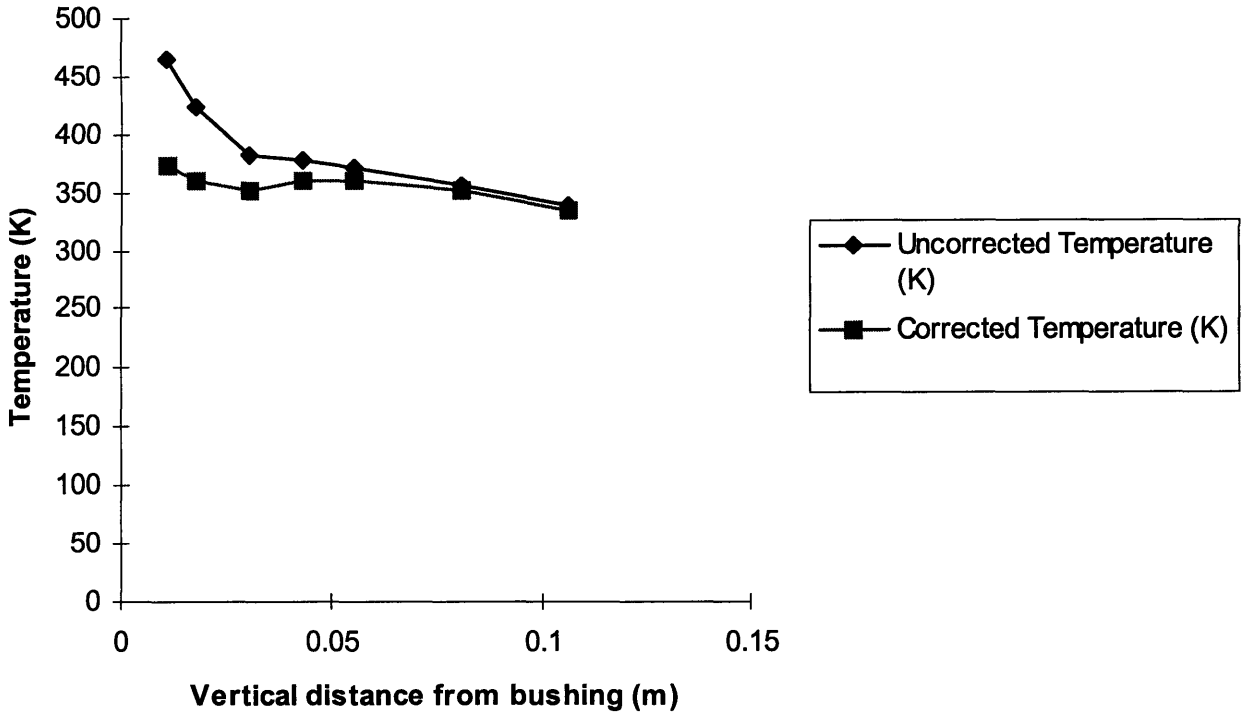

Fig. 5.3.5: Comparison of raw temperature data to the corrected temperature data as a function of vertical distance from the bushing plate. This data is for a nine-tip bushing with a fiber speed of 21.3 m/s, a bushing temperature of 1505 K, and a horizontal position located half way between the left-front and front-center fibers.

It is apparent from figures 5.3.2 through 5.3.5 that there is significant error associated with the raw temperature data, especially at points closer to the bushing plate, where radiation dominates. The raw temperature data are consistently higher than the corrected data, and differences between the raw temperature data and corrected temperature data generally decrease as the vertical position of the thermocouple increases. Based on the model discussed in chapter 4, given no radiation source, conductive losses would result in lower raw temperature data than corrected temperature data; conversely, given a radiation source and no conductive losses, the raw temperature data should be

greater than the corrected data. Since the latter is the type of pattern that has been observed in practice, it is clear that radiation error dominates over conduction error.

The first complete set of air temperature data that will be looked at is that for fiber speeds of 12.2 m/s (40 ft/s). It should be noted that these are corrected temperature values. Compiling all of the temperature data yields the following three-dimensional chart:

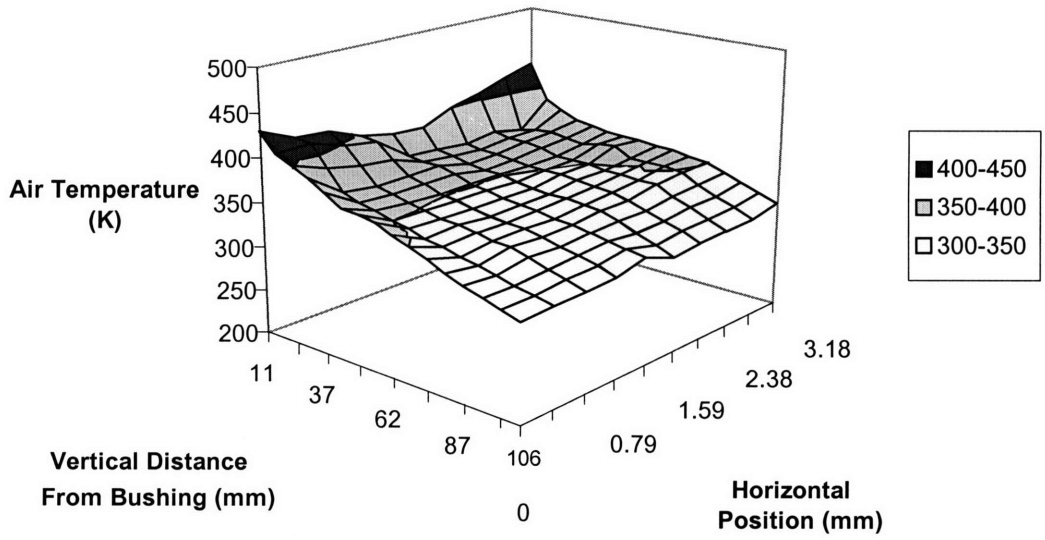

Fig. 5.3.6: Three-dimensional plot of air temperatures for a nine-tip bushing with a fiber speed of 12.2 m/s and a bushing temperature of 1505 K.

It should also be noted that in order to generate this and other three-dimensional plot, some data needed to be interpolated. This was to allow the grid to be evenly spaced. The data may also be viewed in a two dimensional plot, which may assist in seeing the temperature values for individual data points. This data contains no interpolated points:

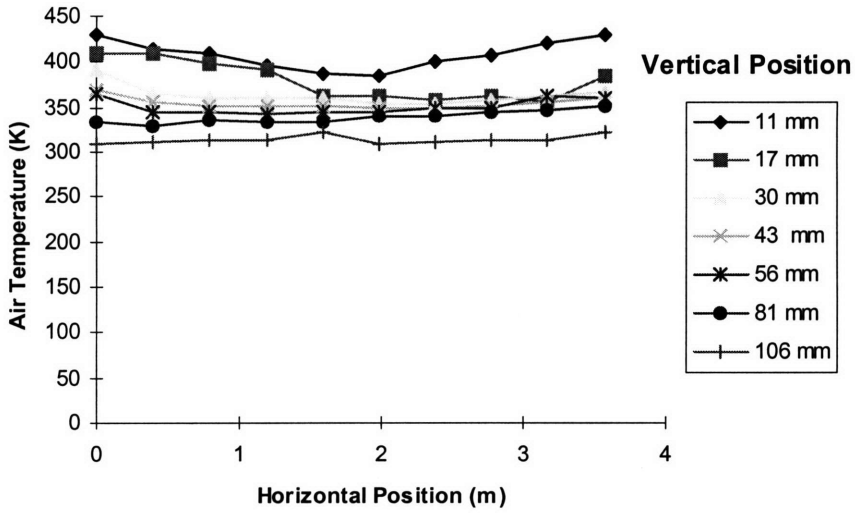

Fig. 5.3.7: Two-dimensional plot of air temperatures for a nine-tip bushing with a fiber speed of 12.2 m/s and a bushing temperature of 1505 K.

It is evident from the preceding plots that as the vertical distance from the bushing plate increases, the air temperature sharply decreases over the first 2 cm or so, and then continues to decrease at a slower and slower rate over the rest of the 10 cm interval. It can also be clearly seen that the air temperatures at points closest to either of the two fibers are generally higher than those at points at farther distances from either of the fibers. These temperature peaks tend to become less and less pronounced as temperatures are measured at points farther and farther vertically from the bushing plate. This type of temperature distribution may be attributed to the convection caused by the forced air flow between the two fibers.

The next data that will be looked at is that for a fiber speed of 15 .3 m/s (50 ft/s), with the same 1505 K bushing temperature. This illustrated in figure 5.3.9:

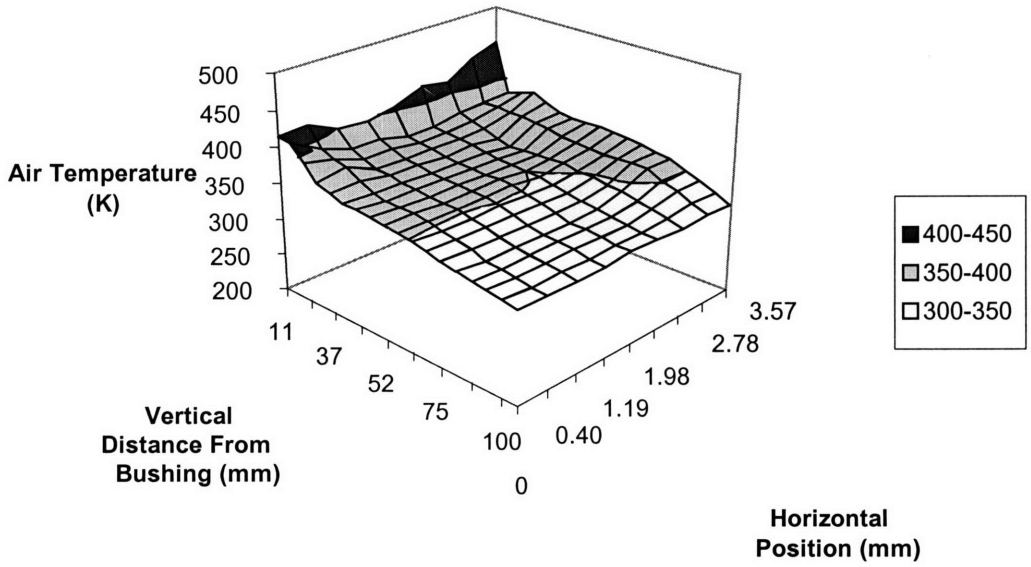

Fig. 5.3.8: Three-dimensional plot of air temperatures for a winder speed of 15.3 m/s and a bushing temperature of 1505 K.

Similarly to the previous data set, it may help to view this data in two-dimensional format:

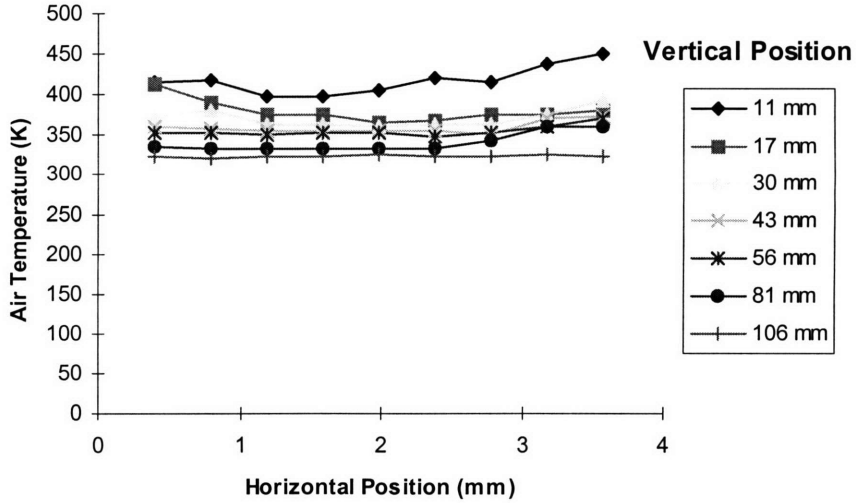

Fig. 5.2.9: Two-dimensional plot of air temperatures for a nine-tip bushing with a fiber speed of 12.2 m/s and a bushing temperature of 1505 K.

This data set shows a very similar pattern to the previous set. The shapes are generally the same. A similar sharper initial temperature drop can be seen as the distance from the bushing plate increases, and also, the air temperatures at points closer to the fibers are slightly higher. A major difference that can best be shown by comparing figures 5.3.6 and 5.3.8 is the higher temperatures on average recorded for the case of the higher fiber speed. This can be seen by comparing the amount of plot area in the 350 K - 400 K temperature range (note the legends). This indicates that there is noticeably more convection coming from the faster traveling fibers (This is despite the fact that the faster-traveling fibers have a smaller diameter than the slower-traveling fibers, as shown in section 5.2)

The final set of air temperature data for the bushing temperature of 1505 K is for a fiber speed of 21.3 m/s. The data is shown in figures 5.3.10 and 5.3.11 below:

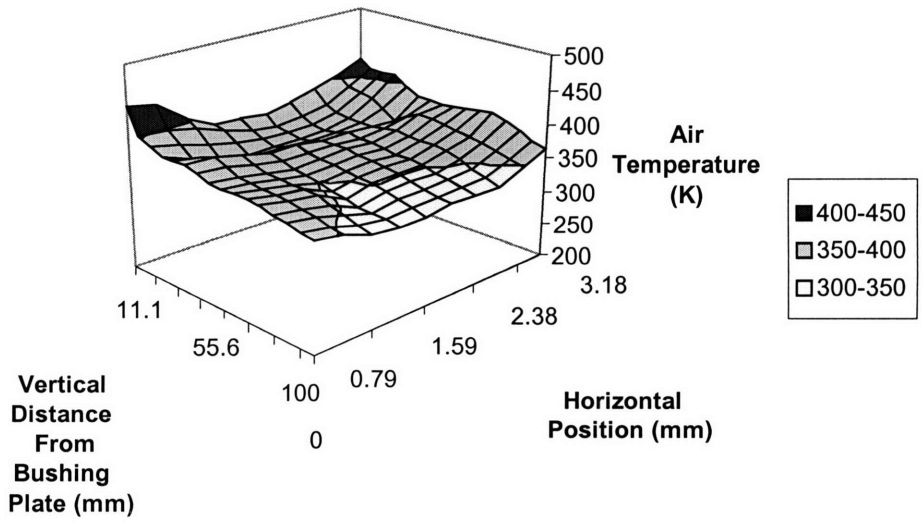

Fig. 5.3.10: Three-dimensional plot of air temperatures for a nine-tip bushing with a fiber speed of 21.3 m/s and a bushing temperature of 1505 K.

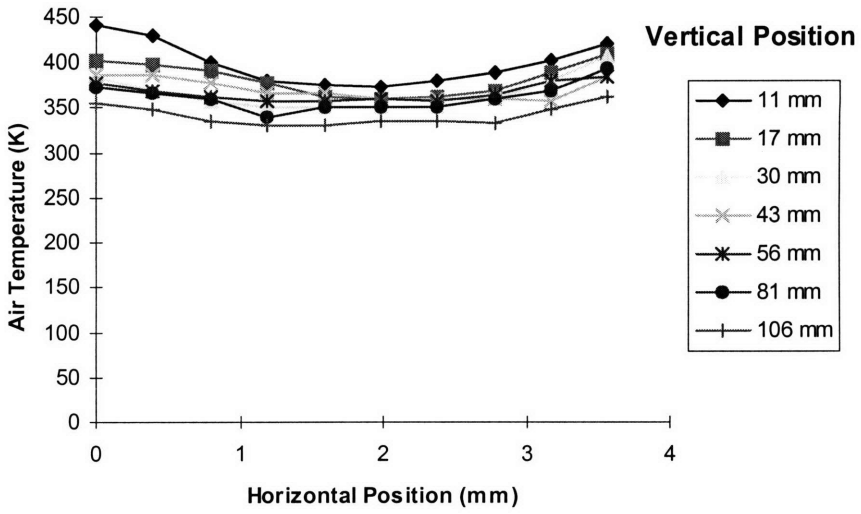

Fig. 5.3.11: Two-dimensional plot of air temperatures for a nine-tip bushing with a fiber speed of 21.3 m/s and a bushing temperature of 1505 K.

Once again, the temperature of the air decreases as the vertical distance from the bushing plate increases, and the temperatures at points nearer to the fibers are generally higher. The major difference is that the level of concavity in figure 5.3.10. Temperatures at points close to the fibers are more highly peaked than the temperatures at the same points for the slower fiber speeds. Also, as the vertical distance from the bushing plate increases, the level of these peaks do not drop off nearly as quickly as was the case for the slower moving fibers. Furthermore, air temperatures on average are significantly higher for this case than for the cases of the slower fiber speeds at the 1505 K bushing temperature. It appears that significantly more convective heat transfer from the fibers to the air is occurs when fibers are drawn at this faster speed, noting that the fiber diameter is even smaller in this case.

It is evident that fiber speed has a noticeable affect on the temperature distribution between two fibers, but it is also important to look at the effects of varying bushing temperature. Data was taken for

bushing temperatures of 1477 K and 1533 K for a fiber speed of 12.2 m/s for a means of comparison to the data for a bushing temperature of 1505 K and a fiber speed of 12.2 m/s presented in figures 5.3.6 and 5.3.7. Figure 5.3.12 is a three-dimensional look at the data for the 1477 K bushing temperature and the 12.2 m/s fiber speed using the nine-tip bushing:

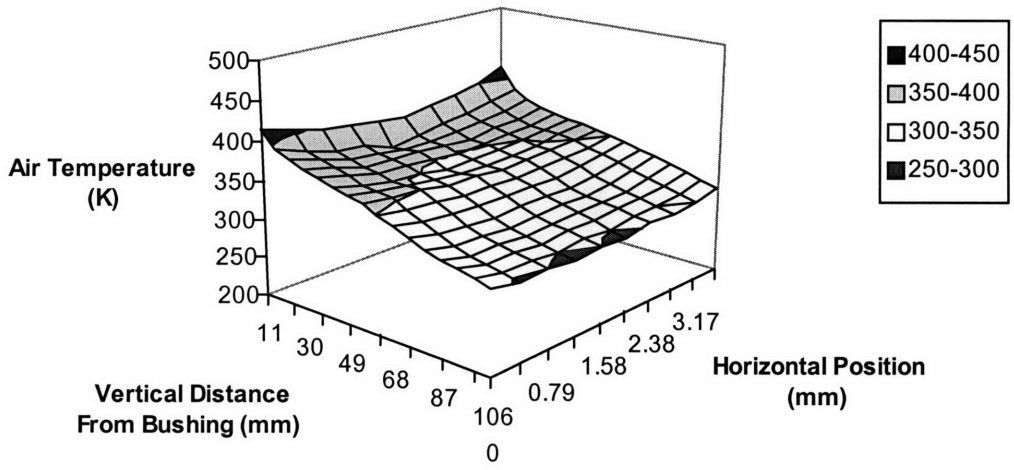

Fig. 5.3.12: Three-dimensional plot of air temperatures for a nine-tip bushing with a bushing temperature of 1477 K and a fiber speed of 12.2 m/s.

As was the case with the previous data, this can also be viewed in two dimensions:

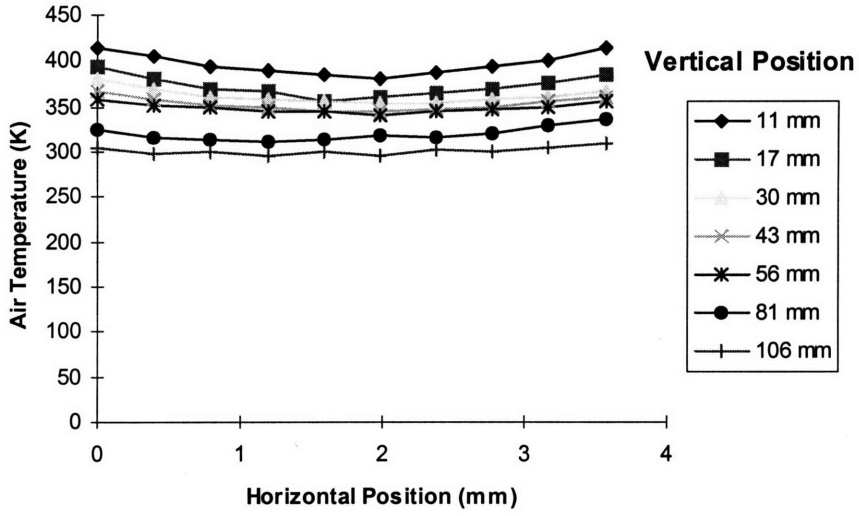

Fig. 5.3.13: Two-dimensional plot of air temperatures for a nine-tip bushing with a bushing temperature of 1477 K and a fiber speed of 12.2 m/s.

Comparing figures 5.3.6 and 5.3.7 to figures 5.3.12 and 5.3.13, respectively, it can be seen that the decrease in bushing temperature results in a slight yet apparent change in the temperature distribution. By comparing the two medium-gray regions of figures 5.3.6 and 5.3.12, it can be seen that the overall air temperatures are slightly lower for the case of the lower bushing temperature. In addition, the temperature peaks at the points in space immediately next to the fibers are less pronounced for the case of the lower bushing temperature. These measurements make sense, since the lower bushing temperature, hence smaller fiber diameter should result in less convective heat transfer from the fibers to the environment.

The next data to look at is that for the same fiber speed of 12.2 m/s and for a bushing temperature of 1533 K. This is shown by the three-dimensional plot in figure 5.3.14 and the two-dimensional plot in figure 5.3.15:

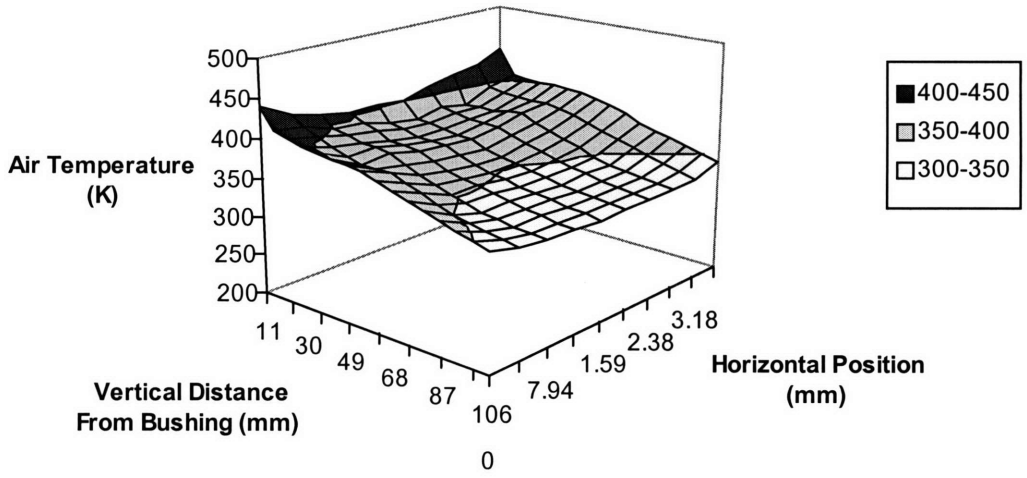

Fig. 5.3.14: Three-dimensional plot of air temperatures for a nine-tip bushing with a bushing temperature of 1533 K and a fiber speed of 12.2 m/s.

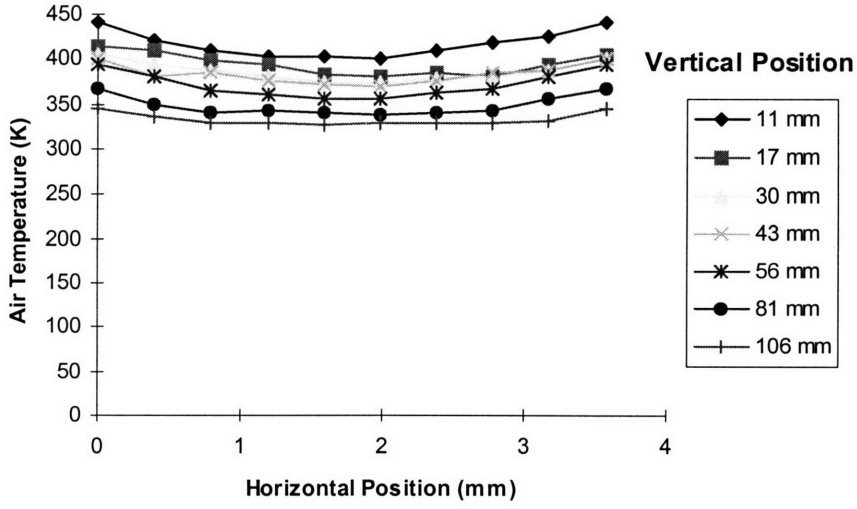

Fig. 5.3.15: Two-dimensional plot of air temperatures for a nine-tip bushing with a bushing temperature of 1533 K and a fiber speed of 12.2 m/s.

Once again, there is a slight difference in the air temperature profile as compared to the case of the data taken with a 1505 K bushing temperature and a 12.2 m/s fiber speed. Comparing the two medium-gray regions in figures 5.3.6 and 5.3.14 shows overall slightly higher air temperatures for the case of the 1533 K bushing temperatures and slightly more pronounced temperature peaks near the points in space closer to the moving fibers.

5.4 Velocity Results

Air velocity data was taken for the same operating conditions at which the temperature data was taken; however, measurements were made at fewer points in space due to the poorer level of resolution available from the pitot tube as compared to the thermocouple. Measurements were made at points between the same two fibers between which the temperature measurements were taken, but only at one point per vertical position. The tube was placed as closely as possible to the left of the center front fiber. Figure 5.4.1 better illustrates this set up:

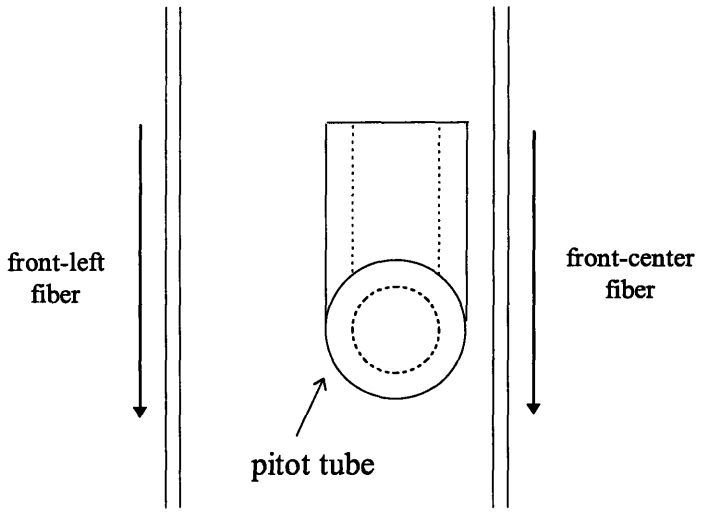

Fig. 5.4.1: Positioning of pitot tube between fibers.

Voltage readings were taken from the pressure transducer that was connected to the pitot tube. These voltages were converted to pressure differences, based on the calibration of the pressure transducer, and were then converted to velocities, based on equation 4.2.2.1. It should be noted that the velocity readings are actually average readings over the area of the opening of the pitot tube. In addition all of the air velocity measurements are vertical (axial) components. Figure 5.4.2 shows these average velocities for different fiber speeds with a bushing temperature of 1505 K:

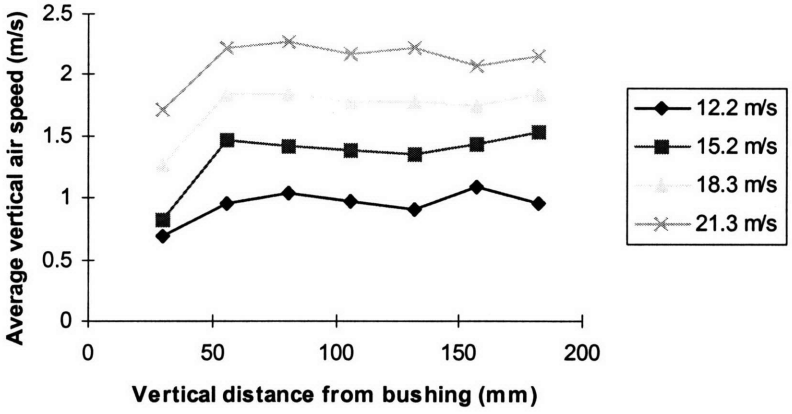

Fig 5.4.2: Air velocities for fiber speeds of 12.2 m/s, 15.3 m/s, 18.3 m/s and 21.3 m/s, using a nine-tip bushing with a bushing temperature of 1505 K.

As should be expected, the measured air velocities increase as the fiber speed increases. Once again, it should be remembered that the increase in fiber speed at a given temperature results in smaller diameter fibers. However, this slight decrease in fiber diameter seems to be outweighed in this case by the speed of the fibers. It also appears that as the vertical distance from the bushing increases, the

measured air velocity initially jumps a bit, but then the increase is more gradual after the distance becomes greater than about 6 cm.

A portion of the same set of data was taken for a bushing temperature of 1533 K. Those results are shown by figure 5.4.3:

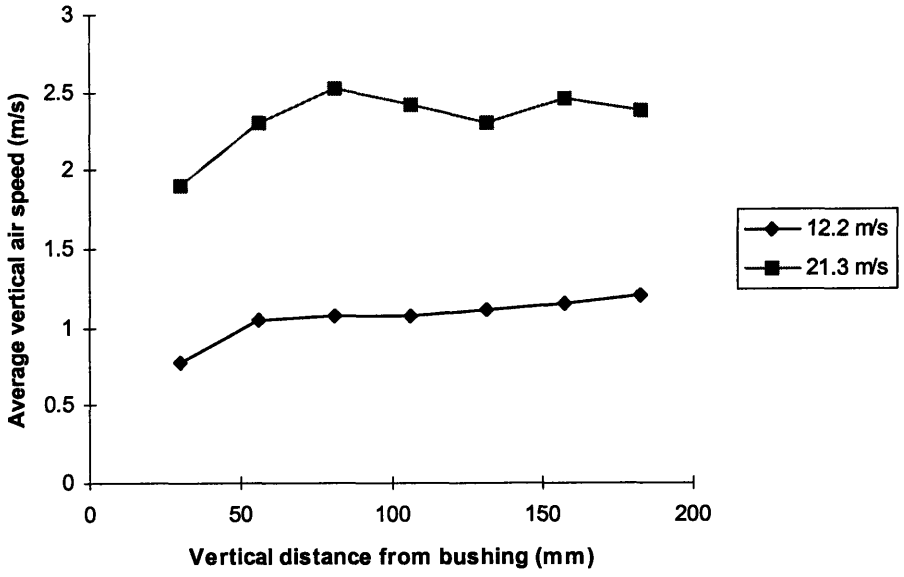

Fig 5.4.3: Air velocities for fiber speeds of 12.2 m/s and 21.3 m/s, using a nine-tip bushing with a bushing temperature of 1533 K.

These results show a nearly identical pattern to those from the case of the bushing temperature of 1505 K. The measurements are a bit higher in this case, but they are fairly close to those of the previous case.

Figures 5.4.4 and 5.4.5 shows, for a given fiber speed, the differences in the air velocity measurements as the bushing temperature is varied.

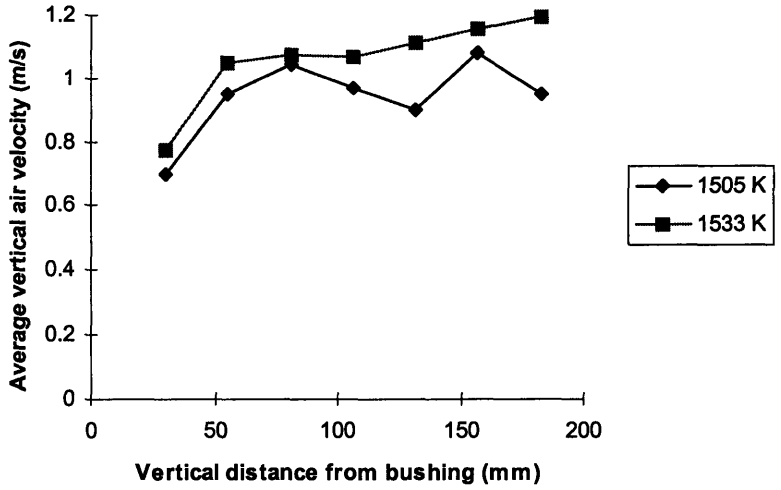

Fig 5.4.4: Air velocities using a nine-tip bushing for bushing temperatures of 1505 K and 1533 K and a fiber speed of 12.2 m/s.

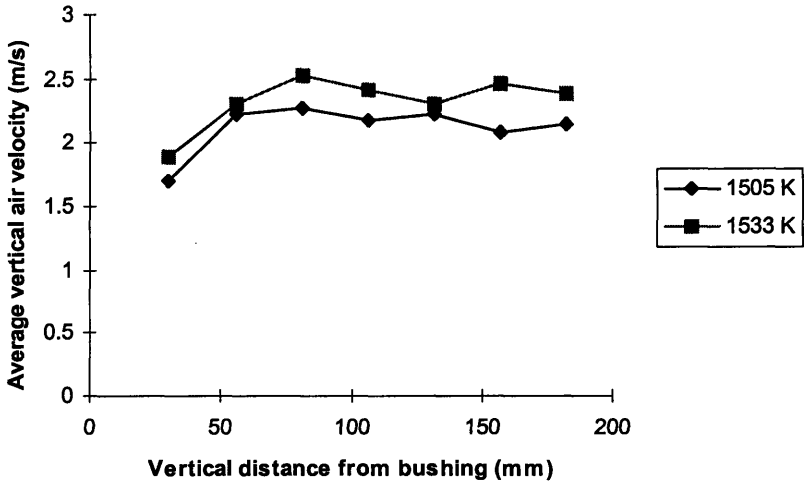

Fig 5.4.5: Air velocities using a nine-tip bushing for bushing temperatures of 1505 K and 1533 K, with a fiber speed of 21.3 m/s.

It is clear from comparing figures 5.4.2 and 5.4.3 to figures 5.4.4 and 5.4.5 that fiber speed has a much more significant effect on air velocities than does the bushing temperature. The main role the bushing temperature plays in this study is as a means of controlling fiber diameter. The data in this section may now be interpreted as showing us that the velocity of the air between the two fibers is much more affected by the speed of the fibers than it is by the diameter of the fibers.

6. Conclusions and Recommendations

There are a number of conclusions that can be drawn from the data obtained in this study. It should be kept in mind that any conclusions that are made are based on a nine-tip bushing arrangement and an environment without water sprays; however, the information obtained nonetheless provides valuable information about the fiber glass forming process.

The first conclusion that can be made based on experimental data is that fiber diameter is greatly affected by both fiber speed and bushing temperature. Bushing temperature, however, appears to have a much greater influence on the diameter of the fiber. Small fluctuations in bushing temperature will yield noticeable variation in fiber diameter, while fiber speed must change much more significantly to yield similar results.

The air temperature data also shows dependence on both fiber speed and bushing temperature. Increasing the fiber speed over a range from 12.2 m/s to 21.3 m/s for a given bushing temperature results in very noticeable changes in the air temperature profile between two fibers. An overall air

temperature increase is observed, in addition to more pronounced peaks in air temperature at points close to the moving fibers. This makes sense because this indicates that there is more convection from the fiber to the surrounding air for faster-moving fibers. The increase in fiber speed results in a decrease in fiber diameter. This should, to some degree, counteract the effects of the increased fiber speed, however given the trends in air temperature that have been observed, the effects of the fiber speed appear to dominate.

Increasing the bushing temperature for a given fiber speed is a way of increasing the fiber diameter. Air temperature data shows that the effects of increasing bushing temperature are similar to those of increasing the winder speed but not quite as significant. It should also be noted that the range of fiber speeds used was much wider than the range of bushing temperatures used, as is the case in production.

Air velocity data shows similar trends to those shown by the temperature data. As fiber speed increases for a given bushing temperature, air velocities also increase, once again, despite the slight decrease in fiber diameter caused by the increase in fiber speed. In addition as the bushing temperature increases, there is a less noticeable increase in air velocities, although it is still observable. The larger size of the fibers caused by the higher bushing temperatures allows the moving fibers to move more air.

There is still much more that can be done to better understand the cooling of glass fibers. More air temperature and velocity data for a greater variety of bushing temperatures and fiber speeds would be useful. In addition it would be beneficial to obtain more such data at more points in space. Also, to try to simplify, if not eliminate the complex temperature correction model by developing a physical means of shielding the thermocouple from the radiation from the bushing would help to streamline the process

of obtaining data. Eventually, it would prove useful to incorporate water sprays into the scaled-down process and to even obtain experimental data using a production scale fiber glass forming position. Furthermore, fiber temperature data would also be extremely helpful, as shown in the analysis in Chapter 2.

Appendix A. Temperature Correction Model

A.1 Introduction

The thermocouple used in this study does not actually directly measure air temperature. It also experiences conductive losses through its leads along with direct heating from the radiation from the bushing plate. These conduction and radiation effects needed to be factored out in order to determine the true air temperature at a particular point in space in the forming environment. The following steady state heat transfer model was used:

$$Q_{radiation} = Q_{convection} + Q_{conduction} . \qquad \text{(A.1.1)}$$

where $Q_{radiation}$ is the radiative heat transfer, $Q_{convection}$ is the convective heat transfer, and $Q_{conduction}$ is the conductive heat transfer. It was assumed that the thermocouple and its wires are under the center

of the bushing plate. Also, to model the conductive losses, the two wires were modeled as a single cylindrical fin with a larger effective diameter.

A.2 Heat Loss Via Conduction Through Leads

For conductive losses:

$$A_c = \frac{\pi D_w^{\,2}}{4}. \tag{A.2.1}$$

$$P = \sqrt{2}\pi D_w. \tag{A.2.2}$$

where A_c is the effective cross sectional area of the fin, i.e the two wires of the thermocouple; D_w is the effective diameter of the fin, which is $\sqrt{2}$ times the actual diameter of a single wire; and P is the total perimeter of the two wires. From here, a fin equation could be developed:

$$k_w A_c \frac{d^2 T_w}{dx^2} - \bar{h}_w P\left(T_w - T_\infty\right) = -q_{rad,w}\frac{P}{2}\alpha_w. \tag{A.2.3}$$

wher k_w is the thermal conductivity of the wire, x is distance along the wire away from the thermocouple bead, $\bar{h}_w$ is the heat transfer coefficient of the wire, T_w is the wire temperature, T_∞ is the

ambient temperature, $q_{rad,w}$ is the radiative heat flux to the wire, and α_w is the absorbtivity of the wire. Solving the differential equation yields the following homogeneous and particular solutions:

$$T_{w,particular} = \frac{q_{rad,w}\alpha_w}{2\bar{h}_w} + T_\infty . \tag{A.2.4}$$

$$T_{w,homogeneous} = Ae^{-x\sqrt{\frac{\bar{h}_w P}{k_w A_c}}} + Be^{x\sqrt{\frac{\bar{h}_w P}{k_w A_c}}} + T_\infty . \tag{A.2.5}$$

where A and B are constants. The second term in the homogeneous solution goes to zero because $|T_w| < \infty$ as x approaches ∞. Since the wire temperature at x=0 is simply the temperature of the thermocouple bead, the following can be stated:

$$T_w(x) - T_\infty = (T_b - T_\infty)e^{-x\sqrt{\frac{\bar{h}_w P}{k_w A_c}}} + \frac{q_{rad,w}\alpha_w}{2\bar{h}_w}\left(1 - e^{-x\sqrt{\frac{\bar{h}_w P}{k_w A_c}}}\right). \tag{A.2.6}$$

And

$$Q_{conduction} = -k_w A_c \left.\frac{dT_w}{dx}\right|_{x=0} . \tag{A.2.7}$$

So

$$Q_{conduction} = \sqrt{\bar{h}_w P k_w A_c}\left[(T_b - T_\infty) - \frac{q_{rad,w}\alpha_w}{2\bar{h}_w}\right]. \quad \text{(A.2.8)}$$

where T_b is the temperature read by the thermocouple, i.e. the temperature of the thermocouple bead. In order to solve for $Q_{conduction}$ it is necessary to first calculate $\bar{h}_w$. For still air, the following natural convection correlation for cylinders may be used:

$$\bar{h}_w = \left(\frac{k_a}{D_w}\right)\left\{0.36 + \frac{0.518 Ra_D^{1/4}}{\left[1+(0.559/Pr)^{9/16}\right]^{4/9}}\right\}. \quad \text{(A.2.9)}$$

with

$$Ra_D = \left(\frac{g\beta}{\nu\alpha}\right) D_w^3 \Delta T. \quad \text{(A.2.10)}$$

where k_a is the thermal conductivity of air, Ra_D is the Rayleigh number based on diameter, Pr is the Prandtl number for air, g is acceleration due to gravity, β is the volumetric coefficient of thermal expansion, and ΔT is the estimated temperature error. For the case of moving air the heat transfer coefficient may be calculated using the following forced convection correlation for cylinders:

$$\bar{h}_w = \left(\frac{k_a}{D_w}\right)\left\{0.3 + \frac{0.62 Re_D^{1/2} Pr^{1/3}}{\left[1+(0.4/Pr)\right]^{1/4}}\right\}. \quad \text{(A.2.11)}$$

with

$$Re_D = \frac{U_\infty D_w}{\nu}. \qquad \text{(A.2.12)}$$

where Re_D is the Reynolds number based on the diameter of the wire, U_∞ is the speed of the moving air, and ν is the kinematic viscosity of air. For slow air speeds, both equations for the heat transfer coefficient yield approximately equal results.

A.3 Radiative Heat Flux

To calculate the radiative heat flux to the thermocouple it was necessary to first find an expression for a view factor in order to make the heat flux due to radiation as a function of the thermocouple's distance below the bushing plate. The thermocouple can be approximated as a small area dA_1. The bushing can be modeled as a square with finite area A_3 and the length of one side equal to $2a$. That means that A_3 is comprised of four smaller square sections of area A_2, each of which have a side of length a. Assuming that the thermocouple is centered underneath A_3, it can be said that this is also where a corner of each of the four A_2's intersect. This approximation is made because the thermocouple is used only in the viscinity of the tips and fibers, which are in at the center of the plate. The following drawing helps in the explanation:

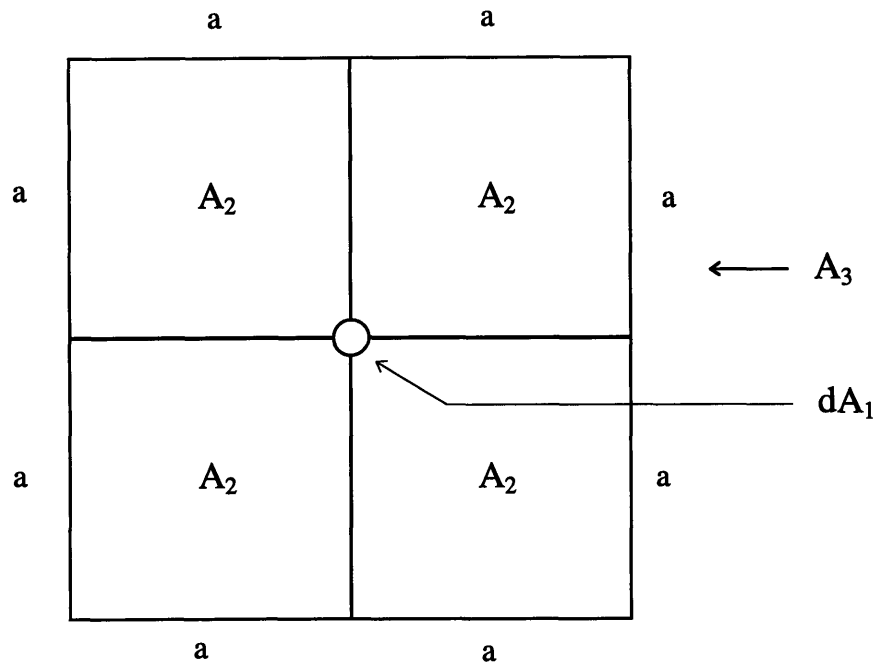

Fig. A.3.1: Illustration for view factor calculation.

The vertical distance between the thermocouple and the bushing plate can be called *c*. From this information, it is possible to calculate a view factor:

$$F_{d1-2} = \frac{1}{\pi}\left\{\frac{\left(\frac{a}{c}\right)}{\left[\left(\frac{a}{c}\right)^2+1\right]^{1/2}} tan^{-1}\left[\frac{\left(\frac{a}{c}\right)}{\left[\left(1+\left(\frac{a}{c}\right)^2\right)\right]^{1/2}}\right]\right\}. \qquad \text{(A.3.1)}$$

Keeping in mind that

$$F_{d1-3} = 4F_{d1-2}. \tag{A.3.2}$$

where F_{d1-3} is the view factor from the thermocouple to the entire bushing plate, and F_{d1-2} is the view factor from the thermocouple to a one-quarter section of the bushing plate. It is now possible to calculate the radiative heat flux from the bushing plate to the thermocouple. The total radiative heat transfer to the thermocouple can be approximated by the following equation:

$$Q_{3\to d1} \cong A_3 F_{3-d1} \varepsilon_3 \sigma T_3^4. \tag{A.3.3}$$

where $Q_{3\to d1}$ is the total heat transfer via radiation to the thermocouple, ε_3 is the emissivity of the bushing plate, σ is the Stefan- Boltzmann constant (5.67 x 10^{-8} W/m^2K^4) and T_3 is the bushing temperature. In this equation, radiation reflected by the bushing plate is neglected, as is radiation lost to the surroundings. Finally, the heat flux to either the thermocouple bead or the wires is represented as follows:

$$q_{rad} = \left(\varepsilon_3 \sigma T_3^4\right)\frac{4}{\pi}\left\{\frac{\left(\frac{a}{c}\right)}{\left[\left(\frac{a}{c}\right)^2+1\right]^{1/2}} TAN^{-1}\left[\frac{\left(\frac{a}{c}\right)}{\left[\left(1+\left(\frac{a}{c}\right)^2\right)\right]^{1/2}}\right]\right\}. \tag{A.3.4}$$

A.4 Convection

The total heat transfer from the thermocouple bead due to convection is shown by the following equation:

$$Q_{convection} = A_b \bar{h}_b (T_b - T_\infty). \tag{A.4.1}$$

with

$$A_b = \pi D_b^{\,2} - \pi D_w^{\,2}. \tag{A.4.2}$$

where A_b, D_b, and $\bar{h}_b$ are the surface area, diameter, and heat transfer coefficient, respectively, of the thermocouple bead. For still air, the following natural convection correlation may be used to calculate the heat transfer coefficient of the spherical bead:

$$\bar{h}_b = \left(\frac{k_a}{D_b}\right)\left\{\frac{0.589 Ra_D^{\,1/4}}{\left[1+(0.559/Pr)^{9/16}\right]^{16/9}}\right\}. \tag{A.4.3}$$

with

$$Ra_D = \left(\frac{g\beta}{\nu\alpha}\right) D_b^{\,3} \Delta T. \tag{A.4.4}$$

where Ra_D is the Rayleigh number based on the diameter of the thermocouple bead. For moving air, one may use the following correlation from forced convection from a sphere:

$$\bar{h}_b = \left(\frac{k_a}{D_b}\right)\left[2 + Pr^{2/5}\left(0.4\,Re_D{}^{1/2} + 0.06\,Re_D{}^{2/3}\right)\right]. \tag{A.4.5}$$

with

$$Re_D = \frac{U_\infty D_b}{\nu}. \tag{A.4.6}$$

where Re_D is the Reynolds number based on the diameter of the thermocouple bead. As was the case for the heat transfer coefficient of the thermocouple leads, for small velocities, both equations for $\bar{h}_b$ will yield approximately equal results.

A.5 Summary

Tying this all together brings us back to equation A.1, the energy balance. Upon substituting terms and simplifying expressions, the following equation is the final result for the error in the thermocouple reading due to radiation from the bushing and conductive losses through the leads:

$$T_b - T_\infty = \frac{\frac{\pi}{2} D_b^{\,2} + \left(\frac{\sqrt{\bar{h}_w P k_w A_c}}{2\bar{h}_w} \right)}{\pi \bar{h}_b \left(D_b^{\,2} - \frac{1}{4} D_w^{\,2} \right) + \sqrt{\bar{h}_w P k_w A_c}} (\alpha q_{rad}). \qquad \text{(A.5.1)}$$

By subtracting this expression for the error from the raw thermocouple reading, it is possible to find a good approximation of the air temperature, T_∞ around the thermocouple.

Bibliography

[1] J.V. Alderson, J.B.Caress, and R.L. Sager,. The cooling rate of glass fiber in the continuous filament process. Laboratory report No. L.R. 235 of Pilkington Bros. Ltd., Lathom, Lancashire, 1968.

[2] C. Ansberg. Massachusetts Institute of Technology, 1999.

[3] R.G.C. Arridge and K. Prior. Cooling time of silica fibers. *Nature*, 203:386-387, 1964.

[4] D.E. Bourne and H. Dixon. The cooling of fibers in the formation process. *Int. J. Heat Mass Transfer*, 24:1323-1332, 1971.

[5] K. Chida and Y. Katto. Conjugate heat transfer of continuously moving surfaces. *Int. J. Heat Mass Transfer*, 19:461-470, 1976.

[6] M.B. Glauert and M.J. Lighthill. The axisymmetric boundary layer on a long thin cylinder. *Proc. R. Soc.*, A320:188-203, 1955.

[7] L.R. Glicksman. The cooling of glass fibers. *Glass Technology*, 9(5):131-138, 1968.

[8] B.H. Kang, J. Yoo, and Y. Jaluria. Experimental study of the convective cooling of a heated continuously moving material. *J. Heat Transfer*, 116(1):199-208, 1994

[9] H.R. Kelly. *J. Aeronautical Sci.*, 21:634, 1954.

[10] R. Madison and P.W. McMillan. The cooling rate of glass fibers. *Glass Technology*, 19(5):127-129, 1978.

[11] A.F. Mills. *Heat and Mass Transfer*. Irwin, Boston, 1995.

[12] B.C. Sakiadis. Boundary-layer behavior on continuous solid surfaces: II. The boundary layer on a continuous flat surface. *A.I.Ch.E. Journal*, 7(2):221-225, 1961.

[13] B.C. Sakiadis. Boundary-layer behavior on continuous solid surfaces: III. The boundary layer on a continuous moving circular fiber. *A.I.Ch.E. Journal*, 7(3):467-472, 1961.

[14] R.A. Seban and R. Bond. Skin friction and heat transfer characteristics of a laminar boundary layer on a cylinder in axial incompressible flow. *J. Aeronautical Sci.*, 18:671-675, 1951.

[15] M. Sweetland. *Nozzle Analysis and Heat Transfer Model for Spray Cooling of Glass Fibers*. Massachusetts Institute of Technology, Cambridge, MA, 1998.

[16] F.M. White. *Fluid Mechanics*. McGraw-Hill, New York, 1986.